PREPRINT UCRL-78729

CONF-761025--3

Lawrence Livermore Laboratory

EXPLODING PUSHER TARGETS ILLUMINATED USING f/1 LENSES AT ∿ 0.4 TW

E. K. Storm, H. G. Ahlstrom, and J. F. Holzrichter

October 5, 1976

This paper was prepared for presentation to the European Conference on Laser Interaction with Matter, Palaiseau, France, October 18-22, 1976.

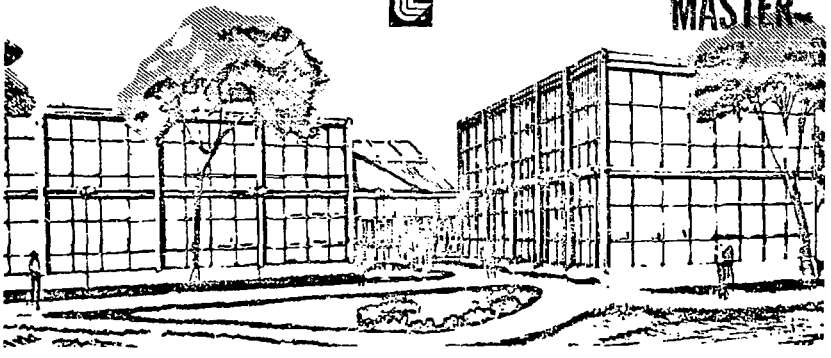

EXPLODING PUSHER TARGETS ILLUMINATED USING f/1 LENSES AT ∿ 0.4 TW

A series of laser fusion microimplosion experiments have been performed with the LLL two beam laser system JANUS[1]. The JANUS laser is capable of focusing up to 400 gigawatts of 1.06 μm laser power (32J in 80 psec) on microscopic laser fusion targets, producing intensities in excess of 10^{17}w/cm^2. In these experiments the targets were Deuterium-Tritium (DT) gas filled, thin walled (.5-1.0 μm) SiO_2 microshells with diameters of 40-100 μm. Targets with these dimensions, properties and laser powers operate in what has become known[22] as the exploding pusher mode. This requires that the laser energy be deposited on a time scale that is short compared with the fluid dynamic implosion time. The elctron thermal wave generated by absorption of laser light in the underdense plasma, propagates supersonically through the glass shell surrounding the DT gas, raising the pressure in the interior of the shell to about one megabar[2]. The shell (pusher) effectively explodes and, thus not only does it expand outward, it also implodes, compresses and heats the DT gas to thermonuclear conditions. Prior to the rapid acceleration of the shell, the DT fuel has been heated to 100-200 eV mainly by electrons (both the electron thermal wave due to the electon conduction from the underdense plasma near the critical density region and by the moderately strong shockwave (∿ 1 megabar) generated by, and running ahead of the imploding (exploding) pusher. Thus, although the final stages of the microimplosion approach an isentropic compression microimplosion, the process as a whole is characterized by a large change in entropy. This is in contrast to the high compression, small entropy change implosion target designs of future experiments and high gain reactor pellets. A summary of the salient points of each design limit is illustrated in the Figure 1.

With present laser outputs in the 100J, 100 psec range, the exploding pusher target offers the possibility of performing low yield laser dirven thermonuclear implosion experiments. It has been shown that this type of target and laser irradiation scheme will not be practical for power generation[23]. However,

it does provide presently achievable experimental conditions which serve as a test bed for computer simulation code development, experimental development of computational models in high power laser plasma interaction physics and diagnostic equipment development.

Because of the importance of this type of target in the early studies of laser fusion feasibility, it was decided to explore a portion of the matrix of parameters that affect the performance of these targets. Among the parameters varied were the SiO_2 microshell diameter, the amount of DT fill in the target, and the time separation of the two laser beams focused on the target. The targets typically absorbed $\sim$ 25% of the 1.06 μm input energy, producing between 10^4 and 6×10^6 neutrons, with the neutron yield scaling inversely with the mass - all other parameters being the same. A detailed derivation of simple scaling rules will be presented in Section III. Of the typically 28J of energy incident upon the target, 7J were absorbed by the target and are collected in the form of plasma and photon energy. Of these 7.0J, 500 mJ were emitted in x-rays between 0.3 and 20 keV. Assuming $A/\bar{Z} \sim 2$, as much as 65% ($\sim$ 4.5J) of the asymptotic ion energy was due to ions with energies exceeding 55 keV, with the remaining energy recovered mainly in a broad distribution of lower ions[3]. A definite asymmetry in the scattered 1.06 μm radiation in and out of the plane of polarization of the incident laser beam was observed[4] together with asymmetric plasma energy[5] distribution, and polarization dependent resonant absorption process[6,7]. Time of flight measurements of the energy distribution of the nominal 3.5 MeV α particles indicate that the reaction products are indeed of thermonuclear origin and are produced from the DT fuel with an effective ion temperature of 2-4 keV[8]. Time integrated x-ray microscope data[9,20] together with time resolved x-ray pinhole pictures[10,21] indicate volume compressions of the order of one hundred produced by the SiO_2 pusher having mean implosion velocities of $\sim$ 2.5×10^7 cm/sec. Similar estimates of the pusher implosion velocity were obtained from the beam delay experiments described in Section IVa and early x-ray streak camera

data[11]. These typical results are also summarized in Table 1.

II EXPERIMENTS

The experiments were performed with the LLL JANUS two-beam laser system. As a detailed description of this system, can be found in Reference 1, only a brief summary will be given here. A passively dye-mode-locked Nd-YAG oscillator produces a single $\sim$ 1 mJ, $\sim$ 75 psec (FWHM), 1.06 μm laser pulse. Through a series of Nd-Glass rod and disc amplifiers with a final output aperture of 85 mm, this pulse is amplified to approximately 30J and focused by two diametrically opposed f/1 lenses (15J per beam). The beam is spatially shaped by an apodized aperture at an early stage of the system to have a "super 5th power Gaussian" profile, $I(r)=I_0 \exp(-r/r_0)^5$. Two bleachable dye-cells (Kodak 9740) in the laser chain protect the targets against damage due to ASE and oscillator prepulse.

Controlling the intensity incuded filamentation instability[12] connected with propagation of high power laser beams through optical materials, is extremely important in producing interpretable and reproducible experiments. An extreme example of this effect is given in Figure 2. Four streak camera images of the laser intensity at the target are shown where the laser energy was increased by a factor of 15 in the sequence with the pulse length constant. The peak intensity in each image has been scaled to the same height. For the last image where small scale beam break up is dominant at the temporal peak of the pulse, we observe that most of the energy is simply missing the focal region. From the point of view of laser fusion targets, this means that the peak power input needed to efficiently drive the implosion process is absent. Considerable care has been taken in staging the JANUS laser to minimize this effect. Presently peak powers of up to 250 GW per beam can be focused onto $\sim$ 80 μm diameter targets with f/1 lenses. However, only experiments with less than $\sim$ 200 GW/beam are included in this report, since filamentation of the beam is becoming important in the distribution of the beam

energy. As part of the diagnostic equipment monitoring the experiments, a 10 psec resolution streak camera[13,19] images the temporal behavior of the focused output beam at a position corresponding to the target plane. This serves both as a measure of the quality of the beam for an individual experiment, and as a measure of the gradual and unavoidable deterioration of the laser system optical components.

Some early results of the laser driven implosion of a DT filled glass microsphere are shown in Figures 3a-3c. Figure 3a shows the target and laser input specifications together with a summary of experimental results and computer code predictions[2]. Figure 3v shows the continuum x-ray spectrum from this target. The typical "two temperature behavior" characteristic of high intensity laser plasma interaction is evident. The portion of the spectrum between 2.5 and 7.5 keV is representative of Bremsstrahlung emission with the slope giving an indication of the plasma electron temperature in the region near the critical density, and the portion of the spectrum above 7.5 keV resulting from suprathermal electrons generated by the non verse Bremsstrahlung laser energy absorption. The computer code simulation of the x-ray spectrum is also shown in this figure. Figure 3c shows an x-ray micrograph[3] of the implosion with emission from the 2.5 keV region of the spectrum. The imprint of the illumination from the two f/1 lenses, and the resulting implosion, compression and heating of the fuel and pusher are clearly discernable. The reasonably close agreement between experiment and computer code simulation gave motivation for doing a series of experiments exploring some of the parameters of the exploding pusher type targets to serve both as a guideline for the direction of future experiments, and to improve our understanding of the physics of these simple laser heating implosion experiments. The matrix of parameters studied in these experiments are summarized in Table II. Section IV of this paper will be devoted to a detailed description of the individual series of experiments and the experimental results.

Even excluding such obvious problems as prepulse damage and beam breakup, the

reliability in reproducing identical laser output parameters makes it imperative to treat each shot as a complete experiment in itself. Due to the complexity of the laser-plasma fluid-dynamic interactions, data juxtaposition from various experiments, is dubious at best. To this end, an extensive diagnostic capability has been developed at LLL for laser fusion experiments. The x-ray emission from the targets is measured from 0.1 to 100 keV with K-edge filtered detectors and curved crystal spectrometers (Lead Stearate, KAP and RAP crystals). The spatially resolved x-ray emission was monitored by a 4 channel grazing incidence x-ray microscope of the Kirkpatrick-Baez[9] type. By combining glass and nickel mirror pairs with appropriate filters, 4 separate energy channels in the .8-3.5 keV region were imaged and absolutely calibrated, with a resolution of $\sim$ 3 μ. Figure 4 shows an example of the rather impressive x-ray emission coverage possible on a typical target shot. Note also the excellent absolute intensity agreement between the various instruments. A 15 psec resolution x-ray streak camera with 7 K-edge filtered channels from 1.6 to 17 keV monitored the temporal x-ray emission from the imploding glass shell[11]. An example of the temporal behavior of the thermal continuum x-rays is shown in Figure 5. A detailed description of the temporal history of an exploding pusher implosion experiment will be given in Section IV. The charged particle flux was measured with ion and electron spectrometers and Faraday cups. An example of the charge collector data and the reduced signal is given in Figure 5. The three peaks in the charge collector signal were seen on all successful shots and appears to be characteristic of the exploding pusher experiments. Figure 7 shows the average of seven electron spectra taken from similar target experiments.

Energy balance measurements were performed utilizing 1.06 μm optical calorimetry and photodiodes which measured the optical energy not coupled to the target. A typical angular distribution of scattered 1.06 μm light is displayed in Figure 8. Both the polarization dependence and the peaking of the distribution in the direction of the focusing lenses are evident. In addition, ion calorimeters[5] measured the

asymptotic ion energy emitted from the target for a number of selected points with respect to the target. Fluor scintillator/PMT combinations measured total thermonuclear neutron and α particle yield and the α particle energy distribution by a time-of-flight measurement[8]. Time integrated optical imaging of the laser target interaction both in the scattered 1.06 μm and 0.53 μ were recorded to aid in the interpretation of the experiments. In addition, the 1.06 μm light transmitted and back reflected from the target was monitored with a 10 psec resolution stream camera[24]. The converging beams from the two f/1 lenses were adjusted such that at the equatorial plane of the target, the beam diameter at the 1/3 intensity points equalled the target diameter. This focusing scheme is much simpler than that employed by KMSF[25,26,27] or the JANUS 4π illumination system [26,29]. Preliminary experiments indicated that, for the JANUS laser, this focusing scheme maximized the implosion symmetry, compression and neutron yield. This focusing scheme was followed for all the target experiments. A typical beam profile showing the time integrated energy density is given in Figure 8. The ring profile observed is due to two effects: The whole beam phase distortion caused by the intensity dependent nonlinear index of refraction effects, and a transition in the beam distribution to $I/I_0 = \exp(-r/r_0)^{12}$ because of the dye cells and a small amount of overfilling in the final two 8.5 cm aperture disk amplifiers in each beam.

III. EXPLODING PUSHER MODELING

A. Results from Lasnex Computer Simulation

From Reference 2 we can extract the following main events or charactertic features of exploding pusher target behavior*.

1. The electron thermal wave[30,14] driven by the absorption of laser light in the underdense plasma, supersonically penetrates the glass shell (pusher) and DT fuel. This raises the pressure on the interior of the shell to about 1 megabar.

---

* (The results were based upon a calculation performed for a 0.45 TW, 50 psec (FWHM) laser pulse focused on a 70 μm diameter SiO_2 microshell with a wall [illegible] and a DT fill of 2 mg/cc).

ii. The shell is thus ready to "jump off," however, before this happens, the following events have taken place. The fuel is heated rapidly to about 0.1 eV both by the electron thermal wave and radiative preheat.

iii. A weak shock wave ($\sim$ 10 K-bars) from the ablation front, heats the fuel to 1-1.5 eV. We note that up until now, the fuel electrons and ions have been closed coupled, since the electron-ion collision times have been relatively short. Using $\tau_{ei} = \frac{3.5\times10^{8}\ AT^{3/2}}{n\ Z^{2}\ \ell n\Lambda}$, we find that for $n \sim 6\times10^{20}$ cm^{-3} (corresponding to 2 mg/cc DT fill and no compression) and $T_e < 1$ eV, $\tau_{ei} \leq 0.15$ psec.

iv. Before the shell "jumps off," electron conduction from the critical density absorption region takes the fuel electrons up to $\sim$ 100 eV. However, now the ions are starting to lag behind, as τ_{ei} increases from 0.15 psec at T_e = 1 eV to 150 psec for T_e = 100 eV.

v. The shell "jumps off" with typical initial implosion velocities of $(1.5\text{-}2)\times10^{7}$ cm/sec. The shell (pusher) has only moved in about 10% of the inital radius at this time, and the typical absorbed energy per unit target mass is $\sim$ 0.04 J/ng.

vi. The pusher is preceded by a moderately strong shock wave (clearly the pusher acts as a piston driving a shock wave into the fuel) of the order of 1 megabar. This heats the fuel ions up to $\sim$ 150 eV and determines the "initial temperation" for the compressional work, $\int pdv$, that follows.

vii. The ion temperature and density now increase due to the compressive work done on the fuel. The electrons do not tract the ions as τ_{ei} continues to be of the order of 50-100 psec for the remainder of process. The fuel electrons are however in close "communication" with the pusher

electrons, and in fact, due to their high thermal conductivity remain at the same temperature as the shell electrons through out the compression phase. As such they do act as an energy loss mechanism for the fuel.

viii. The pusher finally stagnates as the fuel reaches a compression of the order of 100 and ion temperatures of the order of 2 keV, which produces the observed number of thermonuclear reaction products.

B. Simple Target Modeling

Assuming uniform fuel conditions at the time of the thermonuclear reaction, the neutron yield can be written as

$$N = n_D\, n_T\, \langle\sigma v\rangle\, V\tau$$

Here $n_D = n_T$ is the final fuel number density of the D and T ions, and $\langle\sigma v\rangle$ is the Maxwell averaged D-T cross section.

$$n_D = n_T = n_o C$$

$$V \sim r_o^3/C$$

$$\tau \sim \frac{r_o/C^{1/3}}{a_i} \sim \frac{r_o}{C^{1/3} T_i^{1/2}}$$

$$\langle\sigma v\rangle \sim T_i^{\alpha}$$

where

n_o is the inital number density

r_o is the initial radius

C is the volume compression

$a_i \sim T_i^{1/2}$ is the ion speed of sound, and

T_i is the final D-T ion temperature

we find that $N \sim n_0^{2} r_0^{4} C^{2/3} T_i^{\alpha=1/2}$

For simple scaling rules, the task at hand is now to determine how C and T_i depend on the target and the laser input parameters. An inspection of $\langle\sigma v\rangle$ vs T_i shows that for the expected ion temperature range of 1-10 keV that $2.8 < a < 5.5$ so that the success of any simple model depends crucially on an accurate determination of the final DT ion temperature, T_i. Based on the comments in Section IIIa, and the discussion Figure 10, the following assumptions will be made.

1. The final D-T ion temperature is primarily determined by the peak pusher velocity achieved.
2. This peak velocity is basically determined by the ratio of the "useful" energy absorbed, Ec, and the target mass M_T. To be consistent, only that fraction of the shell which implodes, should be used. However, since this is of the order of 40-50% of the total mass this constant will be "absorbed" along with the other numerical constants. Clearly energy which is absorbed after the target has disassembled is not "useful" in producing the peak pusher velocity. Reference 2 was used extensively in developing the scheme to calculate this velocity. From assumptions 1 and 2 we find $T_i \sim E_c/M_T$.
3. Based upon the discussion of Figure 10, the useful energy E_c is defined as

$$E_c = \int_{-\infty}^{t_c} \eta P(t)dt \qquad (4)$$

where P(t) is the laser power, typically of a Gaussian shape and η is the fractional absorption, assumed to be independent of time and is determined experimentally. Typically η=0.25.

The parameter $t_c = t_e + \Delta t_2$ where t_e is the shell explosion or "jump off" time and is defined as $\left(\int_{-\infty}^{t_c} \eta P(t)dt\right)/M_T$ = 0.04 J/ng, and Δt_2 is the time required

for the pusher-fuel interface to travel an additional 20% of the initial radius, $r(t_e)$ is assumed to be = $0.9r_0$. Δt_2 is found by assuming that v(t) is proportional to the square root of the energy absorbed up until that time and solving for

$$\int_{t_e}^{t_e+\Delta t_2} \left\{ \frac{2}{M_T f} \int_{-\infty}^{t} \eta P(\tau) d\tau \right\}^{1/2} dt = 0.2\, r_0 \qquad (5)$$

here f is that fraction of the absorbed energy which goes into the kinetic energy the shell. By normalizing eq. (4) to the data in Figure 10, f was found to be ~ 0.25 for M_T = the total target mass.

A graphic representation of this prescription for finding E_c and a comparison of the resulting pusher-fuel interface trajectory with the Lasnex 1-D simulation, is shown in Figure 12. The solid curve is the 1-D result when the Gaussian input pulse is truncated at the time when the shell has moved in 30% of the initial radius. The dashed lines show the result of applying the prescription outlined above. This model is thus equivalent to assuming that the shell integrates the absorbed energy until the specific energy has reached 0.04 J/ng. At this point the pusher-fuel interface has moved in a distance $0.10\, r_0$ and acquired a velocity proportional to $\sqrt{.04 J/ng}$. It then continues with velocity proportional to the square root of the absorbed energy at any given time. Now to determine a functional relationship for the compression we make the assumption that at $t = t_c$, the inward moving pusher and the fuel are no longer affected by farther absorption of laser energy. We further say that the inward pusher kinetic energy will be converted isentropically to work on the ions. This assumption ignores work done on the electrons and their loss of energy by conduction to the pusher. We also assume that the fuel is stagnated so that all the energy is "thermal." Then for an isentropic compression from t_c to the stagnation condition

$$T_f = T_i\, C^{\delta-1} \qquad (6)$$

where C is the compression.

Using the above assumptions we can write

$$C = 1 + (\delta-1)\,\frac{(KE)_{shell}}{P_e V_e}^{1/\delta-1} \qquad (7)$$

Now we say that

$$C \gg 1$$

$$(KE)_{shell} \sim E_c$$

$$V_c \sim (0.7r_o)^3 \sim r_o^3$$

$$M_T \sim W r_o^2 \qquad \text{where W is the wall thickness}$$

$$P_c = n_c k\, T_c = \frac{1}{0.35}\, n_o k T_c$$

then since T_c is approximately constant and determined by $E_c/M_T = 0.04$ J/ng and for $\delta = 5/3$ we get

$$C \sim (E_c/M_T)\,\frac{W}{r_o n_o}^{2/3} \qquad (8)$$

Combining eq. (2), (3) and (8) we find

$$N \sim n_o r_o^3 W\,(E_c/M_T)^{\alpha+1/2} \qquad (9)$$

We note that the simple dependence on n_o in equation (9) cannot be correct. The yield must certainly increase from zero as the fill, n_o, increases from zero. However, it must finally decrease as n_o becomes large enough to significantly lower then final temperature, T_i. The simple model which we have used to relate T_i to E_c/M_T and to determine E_c did not account for the initial fuel density, i.e. for high enough fuel density our prescriptions for t_e and Δt_2 are not correct. Clearly a more refined model must account for:

i. The final compression is not isentropic and γ is not constant = 5/3 during the compression.

ii. The D-T ion temperature must depend on the compression, and thus $T_i = f(n_o)$

iii. Changing n_0 affects the electron ion collision times and thus the relative importance of the energy loss mechanisms during the compression. It is therefore clear that we have not properly taken into account the dependence on n_0. The question of target performance as a function of D-T fill will be discussed further in Section IV. The model is thus limited to examining scaling behavior for constant D-T fill, and where significant pusher velocities ($\sim 10^7$cm/sec) are achieved. The appropriate model equation is

$$N \sim r_0^3 W (E_c/M_T)^{\alpha+1/2} \qquad (10)$$

to test the validity of the model, the neutron yield was normalized to a specific Lasnex 1-D calculation[2], and the neutron yields predicted from eq. (10) for a large range of target and input laser parameters were compared with the Lasnex 1-D calculations[2]. The results are shown in

figures 13 and 14. The reasonable agreement between this simple model and the detailed Lasnex calculations[2] lends some after-the-fact credence to the simplifying assumptions made during the development eq. (10). It not only suggests that not too much of the physics was "swept under the rug", but that the picture of an exploding pusher that is defined within the limitations of the assumptions is a reasonable one.

IV. EXPERIMENTAL RESULTS

a. Time Delay Series

The first set of experiments discussed are the time delay series. As indicated in Table II, this series of experiments involved delaying the arrival of one converging laser beam focused onto the target, with respect to the other. All of the targets were SiO_2 microspheres with a nominal diameter of 80 μm and wall thickness of 0.7 μm. They were filled with D-T at a density of 2 mg/cc.

Figure 15a shows time integrated x-ray micrograph (in the 2.5 keV region), for the case where there was no delay between the two beams. The imprint of the focused laser beams on the initial position of the 80 μ diameter glass sphere is clearly seen. The final stage of the implosion or the remains of the glass shell at turn-around, is indicated by the x-ray emission from the central portion. The "valley" in the center of the picture shows that, the pressure exerted by the DT gas limited the final linear compression along the optical axis to ~ 7.

Figures 15b and 15d show the effect of delaying one of the beams 42 and 84 psec, respectively, and finally, Figure 15d shows the x-ray micrograph of a target hit by one laser beam only. The deterioration of implosion symmetry is evident. The resulting degradation of neutron yield as a function of beam delay is shown in figure 16. From this result we can obtain one estimate of

the target implosion time scale. Extrapolation indicates that a beam delay of $\gtrsim$ 120 psec is equivalent to a one beam experiment. Conversely, the hydrodynamic implosion time scale is this of the order of 120 psec. Figure 17 shows the variation of the x-ray spectrum as a function of beam delay. A reduction of the high energy spectrum with increasing beam delay is indicated. The asymmetry, of density gradients caused by increasing beam delay is a possible explanation for this phenomena. The arrival of the early beam acts like a prepulse for the opposite side of the target, causing ionization and expansion prior to the arrival of the main pulse for that side. It is likely that the "plasma preparation" reduces the amount of suprathermal x-rays produced by the delayed beam. The apparent hardening of the spectrum (i.e., flattening of the slope of the high energy x-rays) with increasing beam delay is somewhat surprising, and the effect is within the experimental error bars.

Referring back to figure 15, we note the progression of the stagnation region towards the left or the direction of the delayed beam. Microdensitomer scans of the four cases are shown in figure 18. Plotting the position of the center of the stagnation region away from the original center of the target as a function of beam delay, produces Figure 19. From the slope on this x-t plot, we infer a typical pusher implosion velocity of $\sim 2.1 \times 10^7$ cm/sec. Microdensitomer scans of x-ray micrograph pictures like the one shown in figure 15 indicate that the pusher typically travels 30-35 μ before stagnating at peak compression. Combining this with the velocity indicated above, gives another estimate of the hydrodynamic implosion time scale, this one of the order 150 psec. Inspection of figures 15d and 18c, reveals that the pusher in the one sided experiment did not traverse the entire target diameter before stagnating. This is even more obvious upon examining figure 20, which shows the one sided x-ray micrograph image in the 0.8 keV region. The emission from the fluid dynamic convergence point (i.e. where the side that was heated by the laser converges and converts

parts of its kinetic energy to thermal energy before it expands again) is quite distinct, and only a few microns past the original target center. It is also equally clear that after convergence, the, now expanding, pusher only traversed ∿ 60% of the original radial dimension before stagnating. The only reasonable hypothesis is that the back surface acquired sufficient energy to move in ∿ 40% of the initial radius, but not sufficient energy to radiate. Assuming constant pusher velocities for both the front and rear surface, implies that the rear surface must have acquired roughly the equivalent 7.5% of the kinetic energy of the front surface. Or, if we believe in the equipartition of energy, absorbed the equivalent of 7.5% of the incident energy. Detailed Lasnex calculations[2], indicate that this energy was transported from the absorption region by electron conduction through the glass shell.

The scattered light distribution and the electron spectrum, shown in figures 21 and 22 respectively, complete the picture of the time delay series. The polarization dependence of the scattered 1.06 μ light is evident from figure 21. Comparing figure 21 and figure 8, we notice that the effect appears to become more pronounced as the asymmetry of the incident irradiation increases. The hardening of the electron spectrum with increasing beam delay, figure 22, is at the present not well understood.

B. Fill Series

The effect of varying the D-T fill in the targets is most graphically illustrated on figure 23. Here we see x-ray micrographs (all in the 2.5 keV region of the spectrum) of four targets with DT fill of 0, 3, 5 and 7.5 mg/cm^3, respectively. All targets had a nominal diameter of 80 μ and were irradiated by the nominal 35J, 80 psec pulse. The decrease in compression, or inversely, the increase in the distance of closest approach of the converging pusher, is evident. This distance of closest approach, Δ, is normalized by the target

diameter, D and plotted vs D-T gas fill in figure 24. The comment was made in section III, that we could not expect the model the predict the neutron yield variation as a function of D-T fill. This was primarily due to the complex relationship between compression, fill, final temperature and electron-ion coupling times and loss mechanisms. However, within the framework of the model, we would expect that the compression alone, should not deviate significantly from the form indicated by equation 7. The curve predicted by this equation was normalized to the experimental value of Δ/D for the 7.5 mg/cc fill experiment, and is shown in figure 24. The agreement would appear to support the hypothesis made in section III, that in the final stages, the compression approaches the isentropic limit and that is using $\gamma \sim 5/3$ is not totally unreasonable although a $\gamma \sim 3/2$ would probably fit the data just as well. We note that in deriving the equation (same as above), a uniform 1-D compression sequence was assumed. Inspection of figure 23 shows that the actual compression region is oblate with an aspect ratio of about 2:1. The experimental quantity plotted, Δ/D, is proportional to the linear compression along the optical axis, and is thus only a measure of the linear compression. The effect of D-T fill on neutron yield is shown in figure 25. As stated in section III, the model is only capable of predicting the fill effect in a qualitative way. Clearly, for no D-T fill the neutron yield is zero. Increasing the fill from a low value, to first order, we are simply providing more thermonuclear fuel to burn. However, for fixed laser energy on target, a point comes when the increased amount of fuel is offset by the decrease on compression and, consequently, also, in D-T ion temperature. The exact shape of the curve, with the "turn-over" point ocurring at $\sim$ 2 mg/cc fill is predicted by detailed Lasnex calculations[2].

The other experimental data such as electron spectrum, asymptotic ion blow off and scattered light distribution is not shown, for the simple reason that

within experimental error, they showed no significant trends.

C. Size Series

The effect of varying the size of the glass microsphere is illustrated in figure 26. X-ray micrographs (from the 2.5 keV region of the spectrum) show the results from 40, 60, 80 and 100 μ diameter targets, respectively. The tendency towards a more spherically symmetric compression as the initial radius decreases is evident. Since all the targets typically absorbed 20% of the incident energy, the increasing symmetry is most likely a result of the increase in incident laser intensity on the target (W/cm^2). As the inteasity increases, not only do we have a larger heat flux available for transporting the energy around to the equatorial plane, but the temperature gradient also increases. For the 40 μm diameter target, we observe that the conduction efficiency, or conversly, the effective conduction scale length had increased sufficiently to allow conduction to flow around and produce a nearly symmetric implosion.

Since all these targets had the same initial D-T fill, we can use the scaling rules of section VII to predict the variation of neutron yield. This is a rather servere test of the model, since the laser FWHM was essentially kept constant for this size series. The ratio of fluid dynamic implosion time scale to the laser pulse could thus be expected to vary by a factor of ~ 2.5 from the 40 μm to the 100 μm target. The result is shown in figure 27. The solid curve is the model, and the agreement is indeed reasonable. The two solid curves show the effect of varying the laser FWHM and the energy absorbed. For the actual experiments in the size series, the FWHM varied from 50 to 75 psec and the absorbed energy varied from ~ 4 to ~ 6J.

The fraction of energy absorbed as a function of target diameter is shown in figure 28, and is seen to vary from about 23% to 28%.

Using an absorption model that included the effects of resonance absorption

due to parametric decay instabilities, Thomson et.al.[16] computed the expected absorption as a function of target diameter. This is shown in figure 29. The reasonable agreement is additional evidence for the existence and importance of non classical absorption mechanisms for this regime of laser plasma interaction experiments. (We note that absorption due to inverse Bremsstrahlung alone, only accounts for less than 1/5 of the actual absorbed energy).

The x-ray spectrum from the size series is given in Figure 30. The increase both in magnitude and hardening of the high energy tail, with decreasing size is clearly indicated. This trend is to be expected from the increase in intensity at the target surface. Since both the input energy and the laser pulse length were kept constant, we have a six fold increase in intensity in going through the diameter range of these experiments. The dependence of resonant absorption on intensity has been calculated and the hardening of the high energy x-ray spectrum agrees well with code predictions.

D. Other Experimental Results

The first confirmation that the neutrons produced in these experiments came from thermonuclear burn conditions was demonstrated with α particle time of flight measurements.[8] Figure 31 summarizes the principles of the experiment. Experimental ion temperatures of 1.8-3.0 keV were deduced from the thermonuclear burn products by measuring the broadening of the 3.5 MeV α particles. These results are in good agreement with detailed LASNEX calculations.[2]

In the previous sections, neutron yields and x-ray intensities have been discussed based upon normalization by the absorbed energy. The actual absorbed energy was determined in one of two ways. The most accurate and most satisfying from the experimental point of view, involves using the "box calorimeter" shown in figures 32 and 33. This is essentially a total calorimeter that

completely surrounds the target with the exception of holes for the converging laser beams, target insertion and x-ray and side-viewing diagnostics. With conventional calorimeters measuring 1.06 μ energy transmitted and reflected through the f/1 lenses, the box calorimeter covers ∿ 90% of the total remaining solid angle, and measures the optical energy not coupled to the target. The data presented in figures 28 and 29 were based upon measurements made with this calorimeter[5]. Figure 21 shows the percentage of energy absorbed for the three series of experiments. Clearly, using the "box calorimeter" excluded most other diagnostics. In most cases, the energy absorbed was inferred from the optical energy balance. Here, the optical energy not coupled to the target in the solid angle region excluding the two f/1 lenses, was deduced by 15 PIN diodes located in and out of the plane of polarization of the incident beam. Although there is more scatter in this data, the numbers are generally consistent, with ∿ 25% of the incident energy being absorbed[4,5].

From the photodiodes, one can also obtain information on the angular variation of the light that has interacted with the plasma[4]. This has already been shown in figures 8 and 21. A very definite polarization effect is seen, particularly for the one-sided target shots and is consistent with enhanced resonant absorption in the plane of polarization of the incident light.

SUMMARY

Exploding pusher experiments have been performed utilizing the LLL 2 beam laser system, JANUS. A significant fraction of the parameter space that affects the performance of these type of experiments have been explored. A simple model has been developed and when normalized by experiment or LASNEX calculations it can be used to scale results for pulse length, wall thickness, and target radius. It does not produce the proper functional relationship for initial fuel density. The model also illucidates the physical processes occuring in these targets. The salient features of the experiment are listed below:

1. Experiments indicate implosion velocities of (2-3) x 10^7 cm/sec with the magnitude scaling as the useful absorbed energy/target mass.
2. Velocities of (2-3) x 10^7 and (20-60) ng target mass suggest that exploding pusher targets have a relatively poor coupling of absorbed laser energy into hydrodynamic compression.
3. Experiments indicate that the simple scaling of $N \sim W r_0^3 (Ec/M_T)^{\alpha+1/2}$ adequately describes the target performance for fixed D-T fill experiments.
4. The implosion symmetry is greatly enhanced at higher intensities ($\gtrsim 10^{16}$ W/cm^2).
5. Resonance absorption appears to be a significant factor for our focusing of the laser intensity onto the glass shells with f/1 lenses.

REFERENCES

1. D. R. Speck, Laser Program Annual Report-1975, UCRL 50021-75.
2. J. T. Larsen, "Computer Simulation of Laser-Driven Implosion of DT-Filled Glass Microballoons," LLL UCRL 77040, October 1975.
3. V. C. Rupert, Laser Program Annual Report-1975, UCRL 50021-75.
4. D. W. Phillion, R. A. Lerche, V. C. Rupert, K. R. Manes and S. R. Gunn, "Intensity Distribution of the Scattered 1.06 μm Laser Light and Energy Accounting," Bull. Am. Phys. Soc., Vol. 20, No. 10., p. 1286, October 1975.
5. V. C. Rupert, S. R. Gunn, and J. F. Holzrichter, "Energy Absorption by Laser Fusion Targets Determined by Ion Calorimetry," Bull. Am. Phys. Soc., Vol. 20, No. 10., p. 1286, October 1975.
6. W. L. Kruer, R. A. Haas, W. C. Mead, D. W. Phillion and V. C. Rupert, "Collective Behavior in Recent Laser-Plasma Experiments," LLL UCRL 77730, June 1976.
7. K. G. Estabrook, E. J. Valeo and W. L. Kruer, "Two Dimensional Relativistic Simulations of Resonance Absorption," Phys. Fluids, Vol. 18, No. 9, pp. 1151-1159, September 1975.
8. V. W. Slivinsky, H. G. Ahlstrom, K. G. Tirsell, J. Larsen, S. Glaros, G. Zimmerman, and H. Shay, "Measurement of the Ion Temperature In Laser Driven Fusion," Phys. Rev. Lett., Vol. 35, No. 16, p. 1083, October 1975.
9. F. D. Seward, J. D. Dent, M. J. Boyle, L. N. Koppel, T. L. Harper, J. P. Stoering, and A. Torr, "Calibrated "Four-Color" X-Ray Microscope for Laser Plasma Diagnostics," Rev. Sci. Inst., Vol. 47, No. 4, pp. 464-470, April 1976.
10. D. T. Attwood, "Time Resolved X-Ray Pinhole Photography of Compressed Laser Fusion Targets," LLL UCRL 77743, July 1976.
11. D. T. Attwood, L. W. Coleman, J. T. Larsen, and E. K. Storm, "Time Resolved X-Ray Spectral Studies of Laser Compressed Targets," Phys. Rev. Lett., Vol. 37, No. 9, pp. 499-502, (1976).
12. E. S. Bliss, D. R. Speck, J. F. Holzrichter, J. H. Erkkila, and A. J. Glass, "Propagation of a High-Intensity Laser Pulse with Small-Scale Intensity Modulation," Appl. Phys. Lett., Vol. 25, No. 8, pp. 448-450, October 1974.
13. D. T. Attwood and L. W. Coleman, "Picosecond X-Ray Spectral Studies," LLL UCRL 78422, July 1976.
14. Y. B. Zeldovich and Y. P. Raizer, "Physics of Shock Waves and High Temperature Phenomena," Academic Press, New York, Vol. II, Chap. X, p. 421, (1966.
15. K. R. Manes, D. T. Attwood, J. M. Auerbach, J. T. Larsen, D. W. Phillion, and J. E. Swain, "Spherical Microshell Targets Irradiated by the JANUS 4π Illumination System," LLL UCRL 78449, October 1976.
16. E. K. Storm, H. G. Ahlstrom, M. J. Boyle, L. W. Coleman, R. A. Lerche, H. N. Kornblum, D. W. Phillion, F. Rainer, V. C. Rupert, D. R. Speck, and K. G. Tirsell, "Laser Fusion Experiments at 2 TW," LLL UCRL 78581, October 1976.

17. J. E. Swain, E. K. Storm, H. G. Ahlstrom, F. Rienecker, A. J. Glass, J. A. Monjes, K. R. Manes, and D. E. Campbell, "Realities of the JANUS 4π Illumination System," LLL UCRL 78445, September 1976.

18. J. J. Thomson, C. E. Max, J. Erkkila, and J. E. Tull, "Absorption of Focused Light by Spherical Plasmas," LLL UCRL 78315, to be published in the Phys. Rev. Lett, October 18, 1976.

19. D. R. MacQuigg, J. F. Holzrichter, J. T. Hunt, J. E. Swain, D. R. Speck, E. K. Storm, K. J. Pettipiece, "Determination of the Laser Intensity Distribution at the Target in Low f/# Focusing System," Bull. Am. Phys. Soc., Vol. 20, No. 10, p. 1285, October 1975.

20. H. G. Ahlstrom, J. F. Holzrichter, K. R. Manes, E. K. Storm, R. A. Haas, D. W. Phillion, V. C. Rupert, M. J. Boyle, and K. M. Brooks, "Plasma Experiments with 1.06 μm Lasers at the Lawrence Livermore Laboratory," LLL UCRL 77943 (Revision 1), September 1976.

21. D. T. Attwood, L. W. Coleman, M. J. Boyle, D. W. Phillion, J. E. Swain, K. R. Manes, and J. T. Larsen, "Spatially and Temporally Resolved X-Ray Emission from Imploding Laser Fusion Targets," LLL UCRL 78434, September 1976.

22. G. H. Dahlbacka and J. H. Nuckolls, "Laser Driven Isothermal Implosions," LLL UCRL 75885, October 1974.

23. J. H. Nuckolls, L. L. Wood, A. R. Thiessen, and G. B. Zimmerman, "Laser Compression of Matter to Super-High-Densities; Thermonuclear (CTR) Applications," Nature (Lond.), Vol. 239, pp. 139-142, September 1972.

24. R. A. Haas, W. C. Mead, W. L. Kruer, D. W. Phillion, H. N. Kornblum, J. D. Lindl, D. MacQuigg, V. C. Rupert, and K. G. Tirsell, "Irradiation of Parylene Disks with a 1.06 μm Laser," LLL UCRL 77930, June 1976.

25. G. Charatis, J. Downward, R. Goforth, B. Guscott, T. Henderson, S. Hildum, R. Johnson, K. Moncur, T. Leonard, F. Mayer, S. Segall, L. Siebert, D. Solomon, and C. Thomas, "Experimental Study of Laser-Driven Compression of Spherical Glass Shells," Plasma Physics and Controlled Nuclear Fusion Research-1974, Vol. II, Session VIII, pp. 317-335, November 1974.

26. C. E. Thomas, "Laser Fusion Target Illumination System," Applied Optics, Vol. 14, No. 6, pp. 1267-1273, June 1975.

27. J. G. Downward, "Experimental Measurement of the Intensity Variation of Reflected Energy from Spherical Glass Laser Targets," Bull. Am. Phys. Soc., Vol. 19, No. 9, pp. 886-887, October 1974.

28. E. K. Storm, H. G. Ahlstrom, J. A. Monjes, J. E. Swain, V. C. Rupert, and D. W. Phillion, "Exploding Pusher Experiments Utilizing a 4π Illumination System," LLL UCRL 78730, October 1976.

29. R. E. Marshak, "Effect of Radiation on Shockwave Behavior," Phys. Fluids, Vol. 1, No. 1, pp.24-29, January-February 1958.

TABLE I

TYPICAL RESULTS FOR EXPLODING PUSHER LASER FUSION TARGETS

Incident Energy (2 beams)	28J, 75 psec
Absorbed Energy	7J
Number of 14.1 MeV neutrons	$\sim 10^6$
D-T Ion Temperatures from α-particle Time-of-Flight	(1.5 - 2.5) keV
X-Ray Energy .3 keV < $h\nu$ < 17 keV	$\sim$ 0.1J
Ions	Assuming A/Z=2, up to $\sim$ 65% of absorbed energy is recovered in ions with > 55 keV

Ratio of light scattered $\perp$ and $\parallel$ to plane of polarization of incident light can be as high as 4:1.

Real Pusher Implosion Velocities $\sim 2.5 \times 10^7$ cm/sec.

TABLE II

EXPERIMENTAL MATRIX FOR EXPLODING PUSHER LASER FUSION TARGETS

All experiments done using JANUS 1.06 μ Nd-Glass laser, with the focusable power per beam ∿ 0.2 TW.

All targets were SiO_2 DT filled glass microspheres with a wall thickness of ∿ 0.6 μm - 1.0 μm.

Experimental Series #1: Beam Simultaneity

Diameter ≃ 80 μm, D-T fill = 2 mg/cc

Delay one beam relative to the other (delay ≡ Δt) 42, 84 and ∞ psec

Experimental Series #2: Target Fill

Diameter ≃ 80 μm, No time delay (Δt< 3 psec)

Vary the D-T fill from 0 - 8 mg/cc

Experimental Series #3: Target Size

D-T fill = 2 mg/cm³, No time delay (Δt< 3 psec)

Vary the microsphere diameter from 40-100 μm

	Exploding pusher	Isentropic, high density
Fluid dynamic instabilities	Not sensitive	Critical
Plasma instabilities	Not sensitive	Critical
Entropy change	Large	Minimal
Pulse shaping	Not required	Required
Target manufacturing tolerances	Low	High
Implosion velocities	$\sim 5 \times 10^7$ cm/sec	$\sim 5 \times 10^7$ cm/sec
Density	$\sim 1 - 10$ g/cm^3 (peak density achievable)	~ 1000 g/cm^3 (required for efficient burn)

9/76

Figure 1

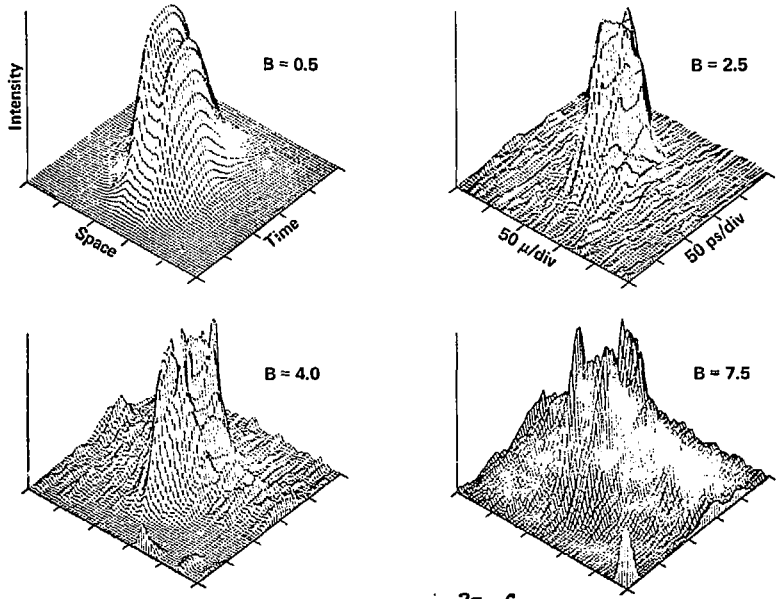
Intensity
B = 0.5
Space
Time
B = 2.5
50 μ/div
50 ps/div
B = 4.0
B = 7.5
$I(k) = I_0(k)e^B$
$B = \frac{2\pi}{\lambda_{vac}} \int \gamma l d\ell_{glass}$

Figure 2

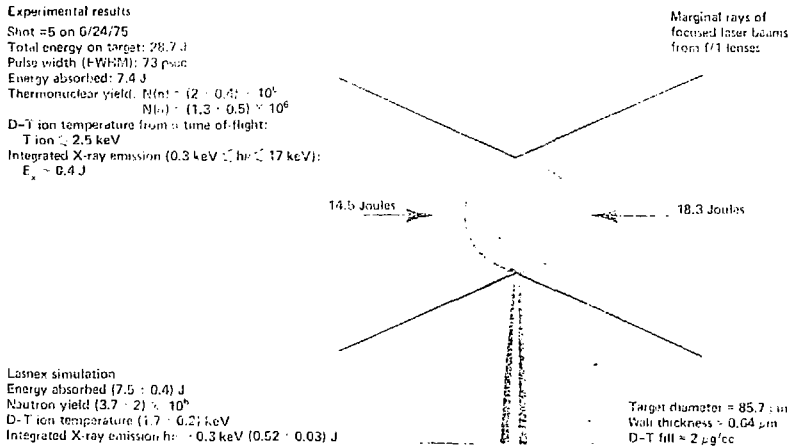
Experimental results
Shot =5 on 6/24/75
Total energy on target: 28.7 J
Pulse width (FWHM): 73 psec
Energy absorbed: 7.4 J
Thermonuclear yield: N(n) = (2 ± 0.4) × 10^5
N(p) = (1.3 ± 0.5) × 10^6
D–T ion temperature from time of-flight:
T ion ≈ 2.5 keV
Integrated X-ray emission (0.3 keV ≤ hν ≤ 17 keV):
E_x ≈ 6.4 J
Marginal rays of
focused laser beams
from f/1 lenses
14.5 Joules
18.3 Joules
Lasnex simulation
Energy absorbed (7.5 ± 0.4) J
Neutron yield (3.7 ± 2) × 10^5
D-T ion temperature (1.7 ± 0.2) keV
Integrated X-ray emission hν > 0.3 keV (0.52 ± 0.03) J
Target diameter = 85.7 μm
Wall thickness ≈ 0.64 μm
D–T fill ≈ 2 μg/cc

Figure 3a

CONTINUOUS X-RAY SPECTRA

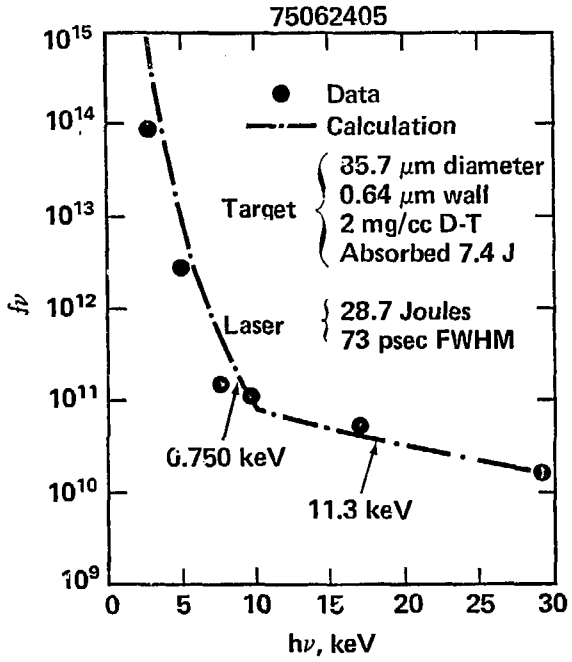

9/76

Figure 3b

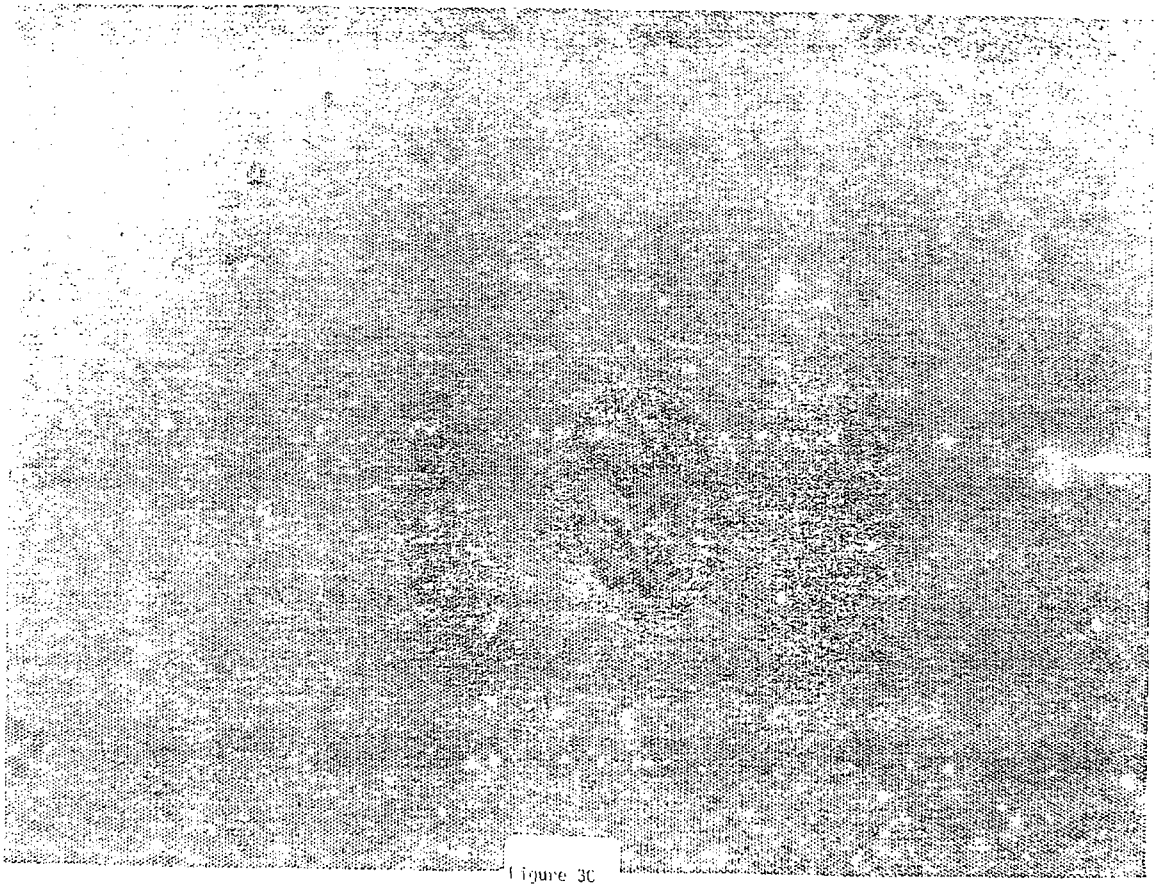

Figure 30

B-17 MICROBALLOON X-RAY SPECTRAL DATA

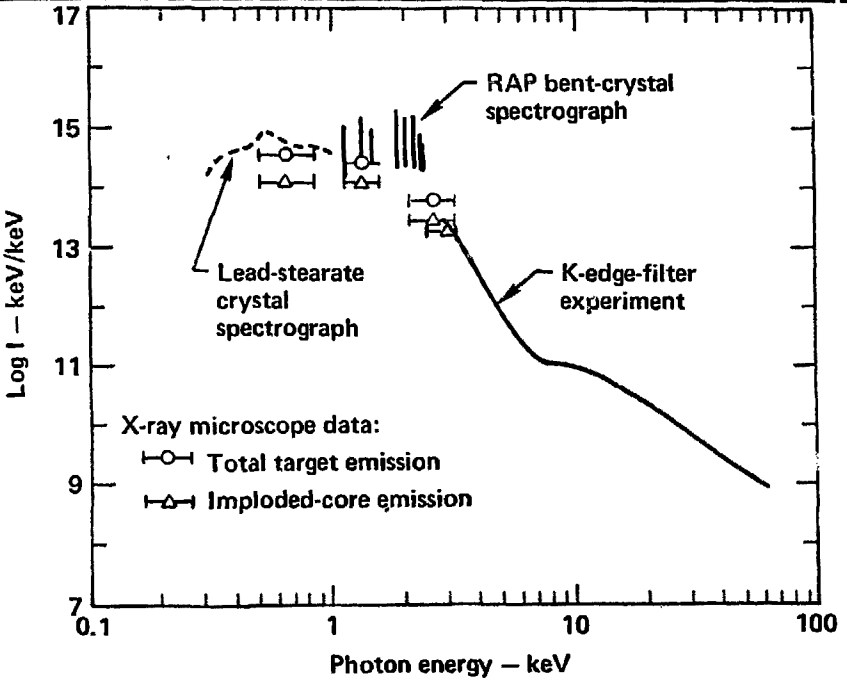

Figure 4

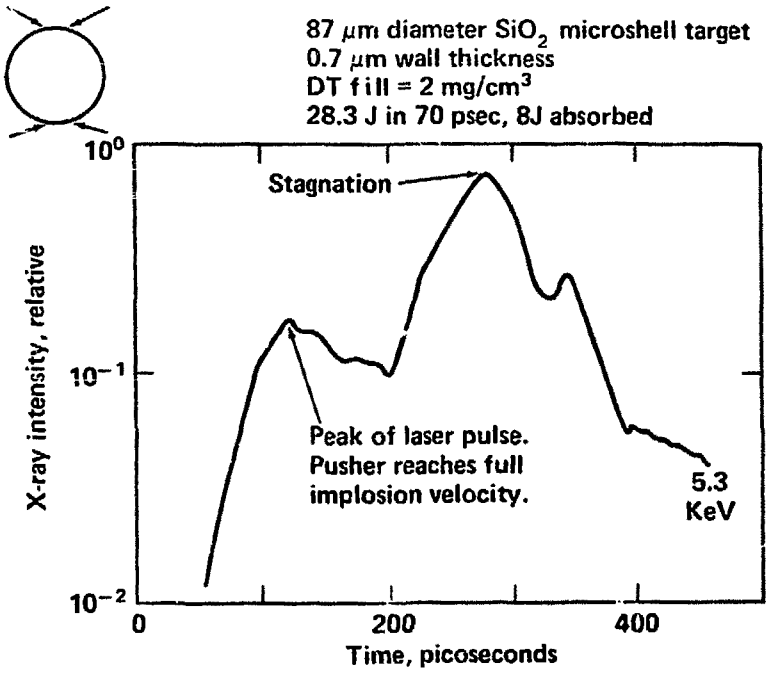
87 μm diameter SiO_2 microshell target
0.7 μm wall thickness
DT fill = 2 mg/cm³
28.3 J in 70 psec, 8J absorbed
10^0
10^{-1}
10^{-2}
X-ray intensity, relative
Stagnation
Peak of laser pulse.
Pusher reaches full
implosion velocity.
5.3
KeV
0
200
400
Time, picoseconds

Figure 5a

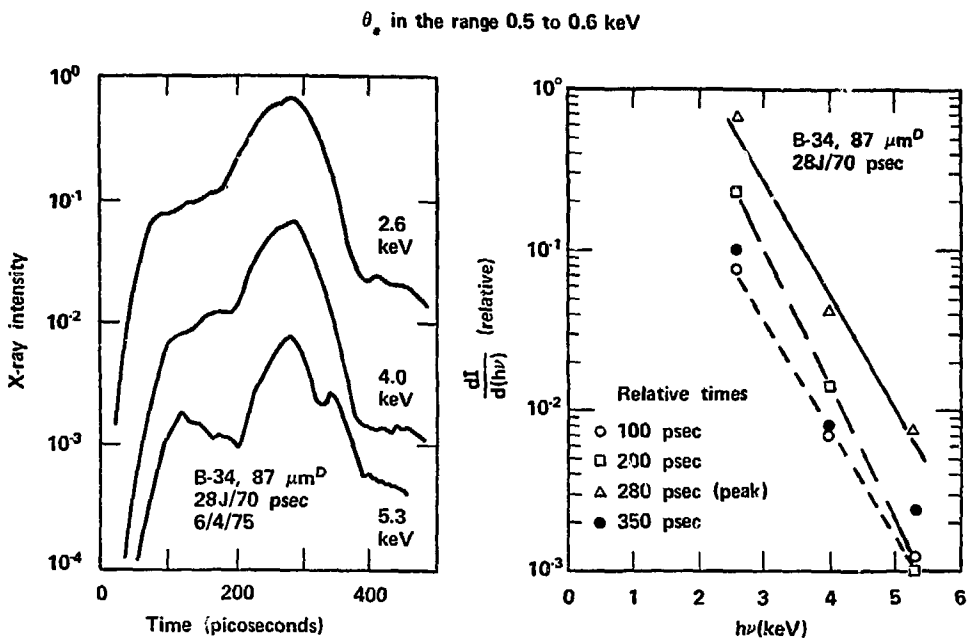
θ_e in the range 0.5 to 0.6 keV
X-ray intensity
Time (picoseconds)
2.6 keV
4.0 keV
5.3 keV
B-34, 87 μm^D
28J/70 psec
6/4/75
$\frac{dI}{d(h\nu)}$ (relative)
$h\nu$(keV)
B-34, 87 μm^D
28J/70 psec
Relative times
100 psec
200 psec
280 psec (peak)
350 psec

Figure 5b

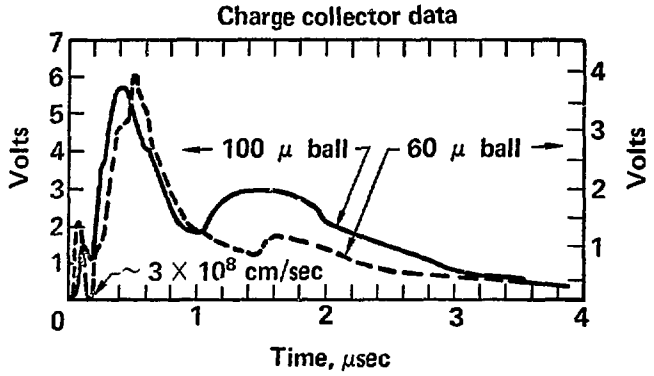
Charge collector data
Volts
Volts
100 μ ball
60 μ ball
~ 3 X 10^8 cm/sec
Time, μsec

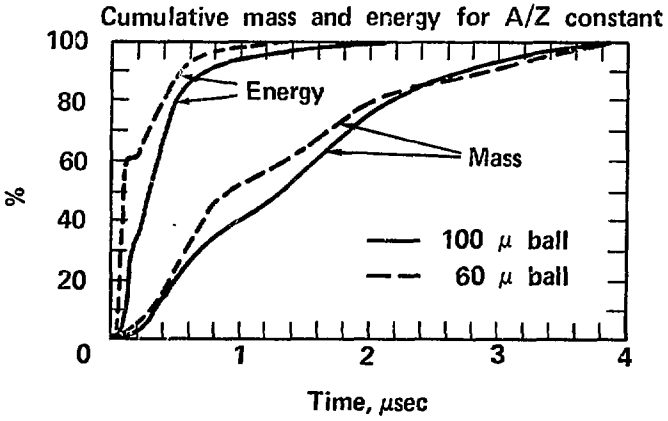
Cumulative mass and energy for A/Z constant
%
Energy
Mass
100 μ ball
60 μ ball
Time, μsec

Figure 6

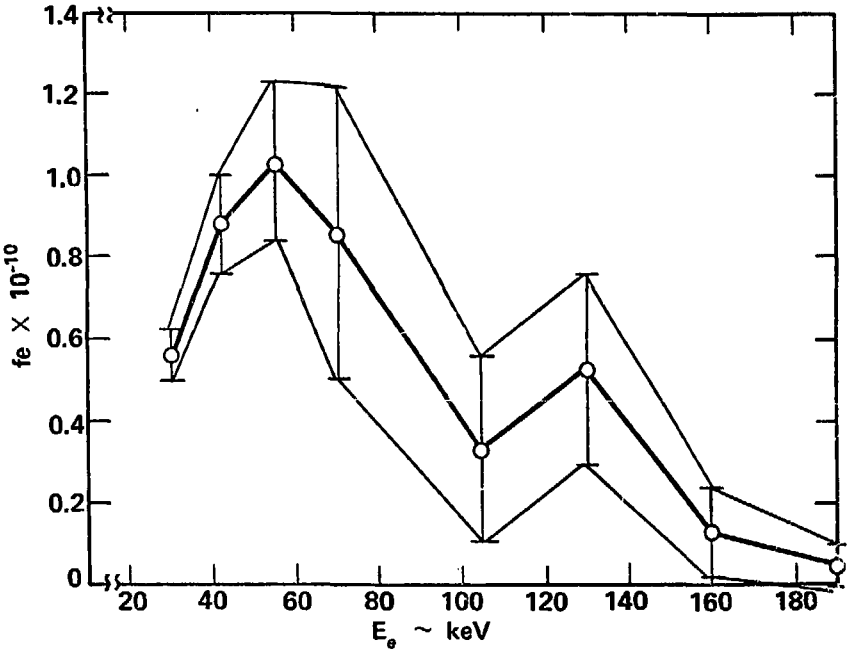
1.4
1.2
1.0
0.8
0.6
0.4
0.2
0
fe X 10-10
20
40
60
80
100
120
140
160
180
Ee ~ keV

Figure 7

THE SCATTERED 1.06 μ LIGHT SHOWS POLARIZATION DEPENDENCE

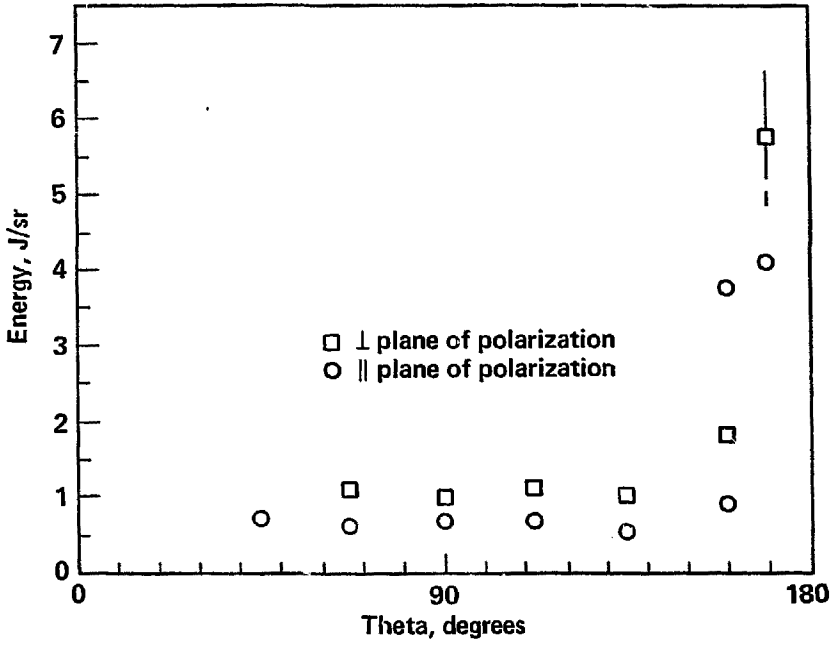

9/76

Figure 8

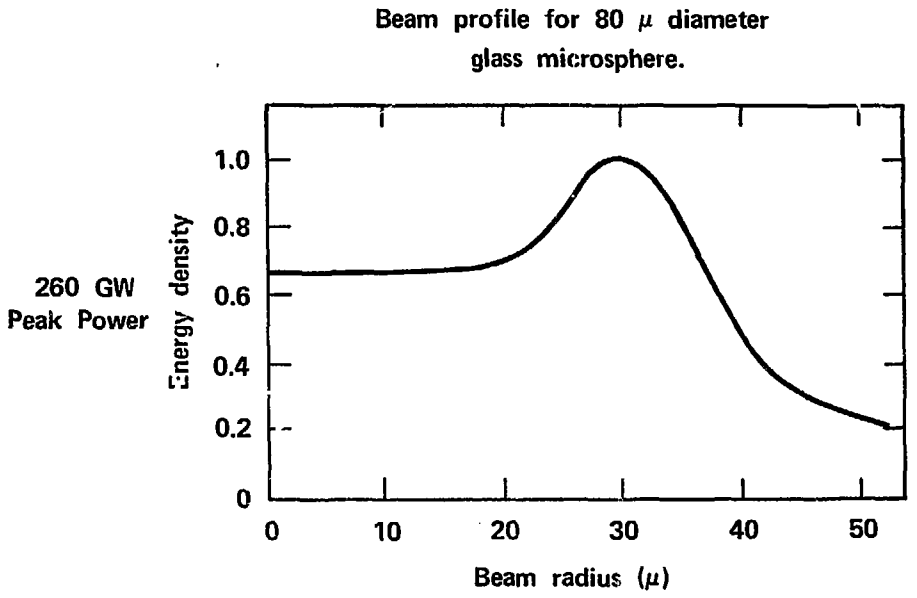
Beam profile for 80 μ diameter
glass microsphere.
260 GW
Peak Power
Energy density
1.0
0.8
0.6
0.4
0.2
0
0
10
20
30
40
50
Beam radius (μ)

Figure 9

LASNEX 1-D TARGET PERFORMANCE

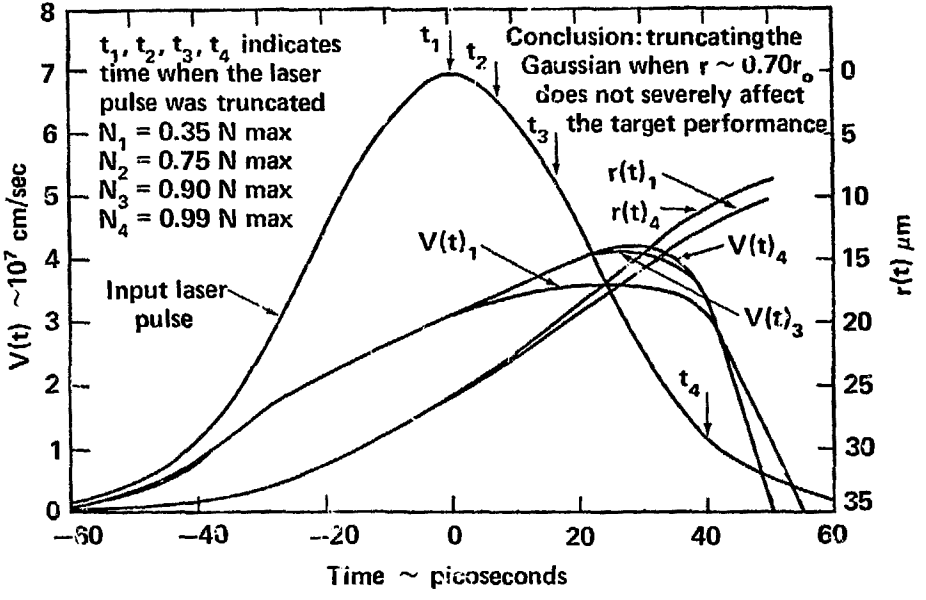

Figure 10

PUSHER/FUEL INTERFACE TRAJECTORY-SPHERICAL ILLUMINATION EXPERIMENT VS LASNEX I-D SIMULATION

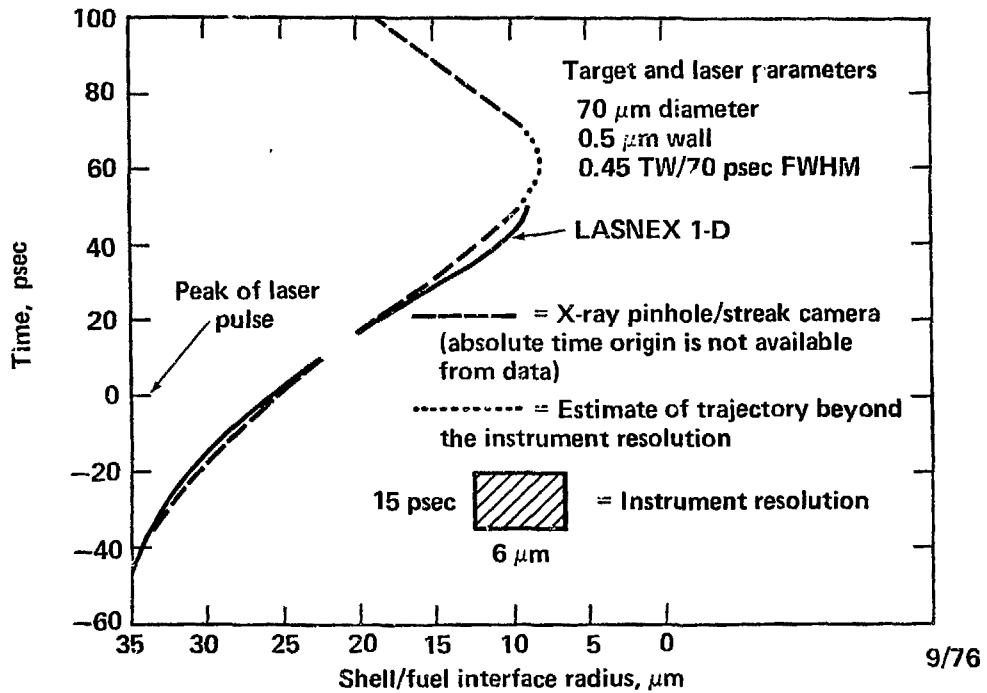

Figure 11

VELOCITY AND r-t TRAJECTORY FOR THE SIMPLE MODEL

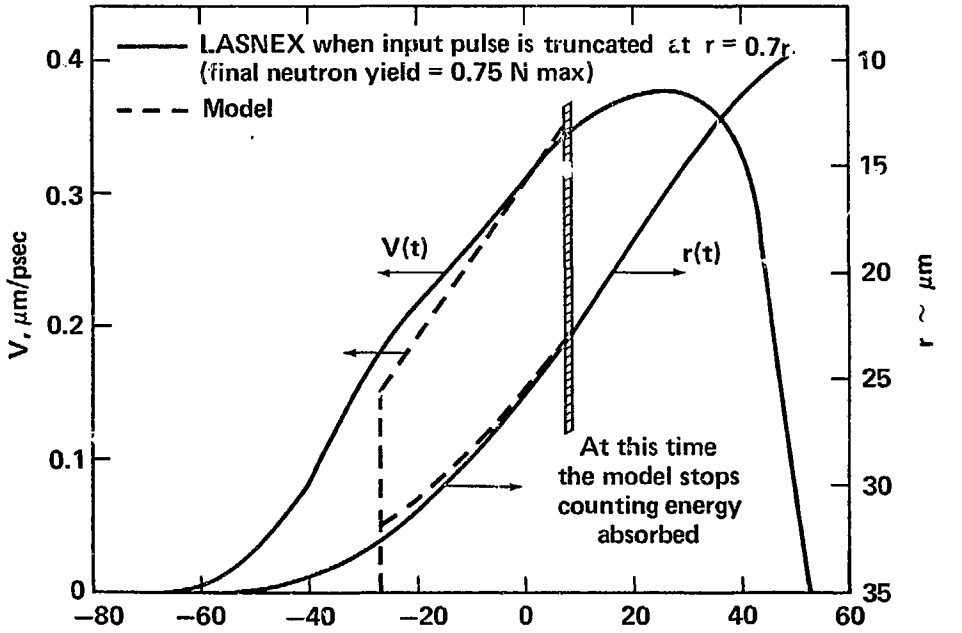

9/76

Figure 12

EXPLODING PUSHER NEUTRON YIELD AS A FUNCTION OF TARGET DIAMETER AND WALL THICKNESS

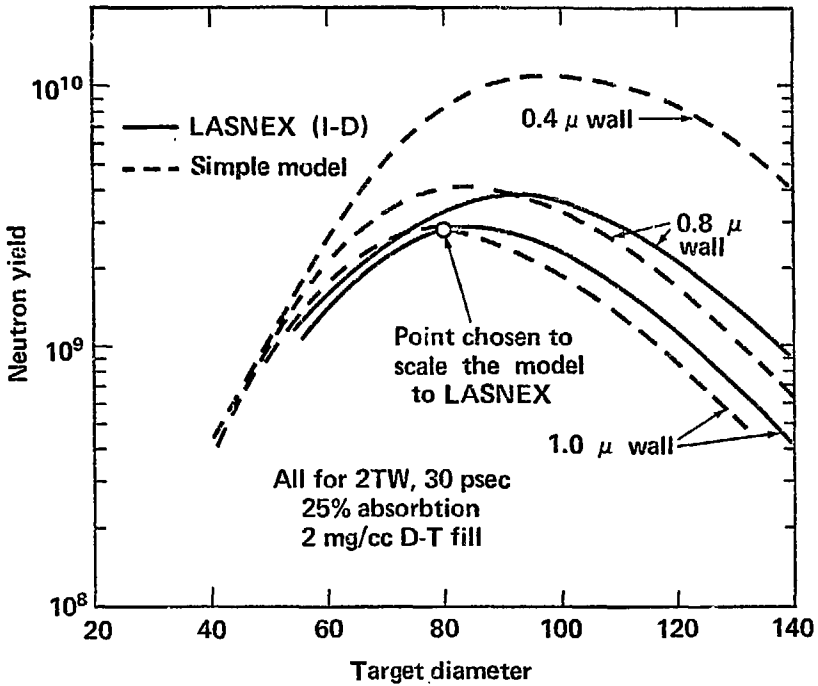

9/76

Figure 13

THE SIMPLE MODEL TRACKS LASNEX I-D SIMULATIONS OVER 6 DECADES IN NEUTRON YIELD

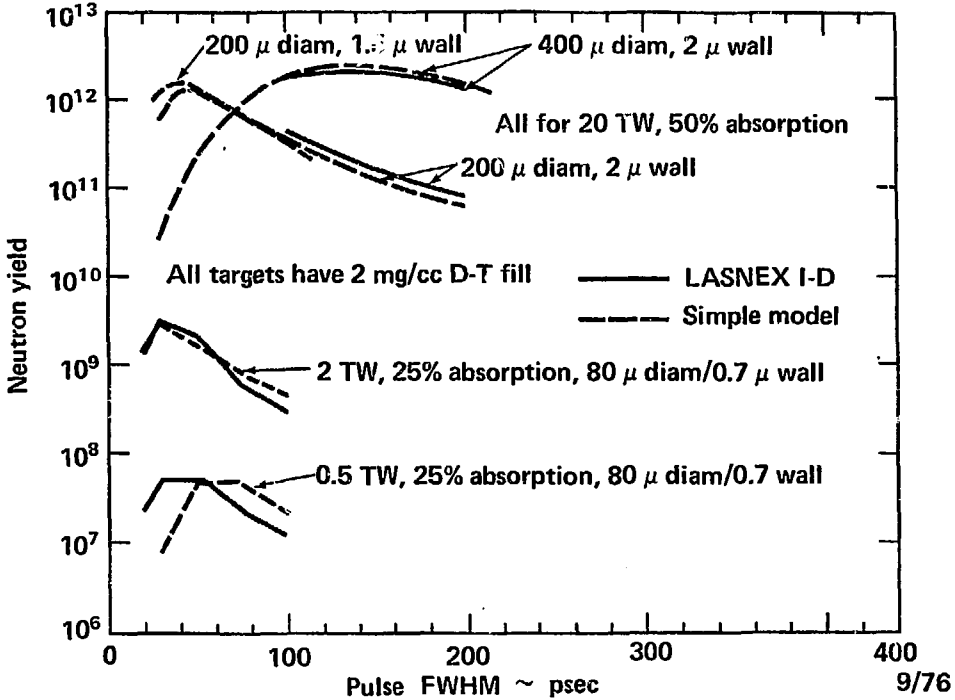

Figure 14

MISMATCH IN BEAM SIMULTANEITY IS DRAMATICALLY DISPLAYED BY X-RAY MICROGRAPHS

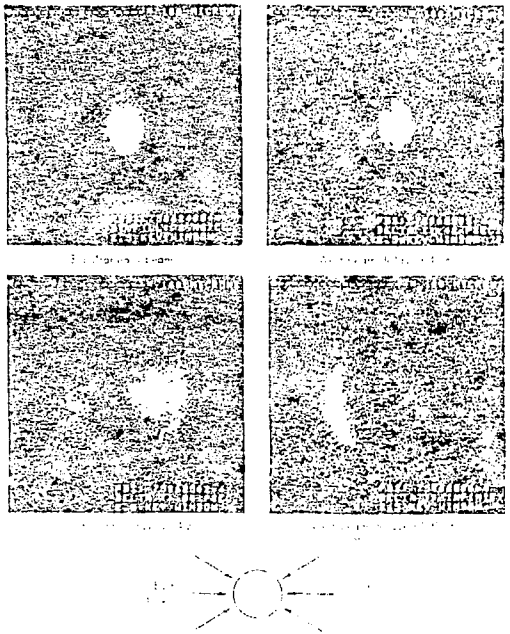

FIGURE 15

Extrapolation tells us that a beam delay $\gtrsim$120 psec is equivalent to one beam operation

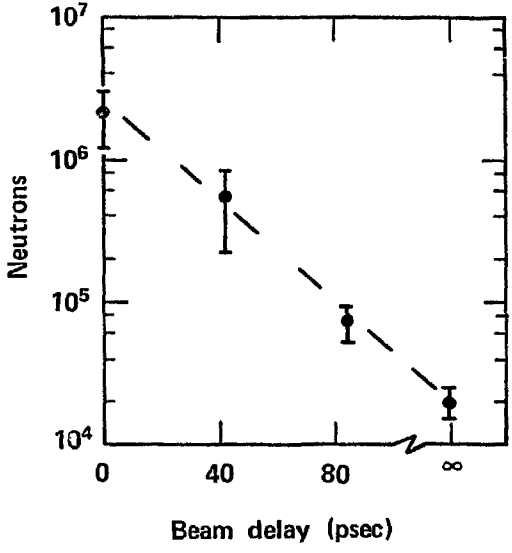

Figure 16

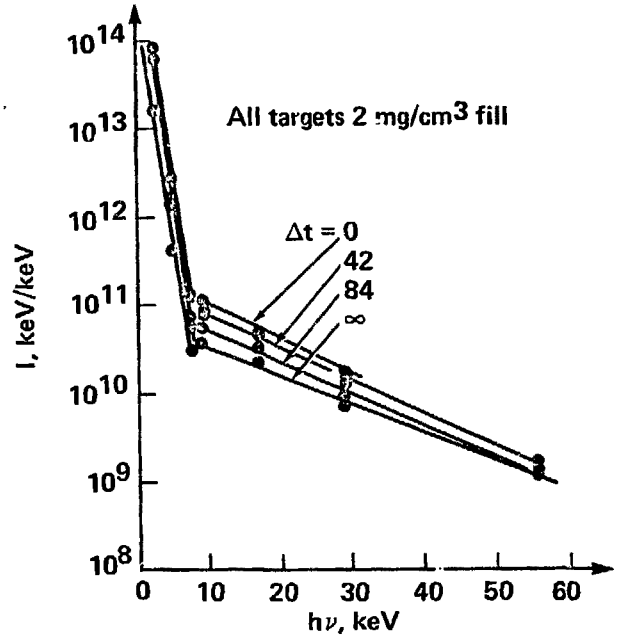
All targets 2 mg/cm3 fill
Δt = 0
42
84
∞
I, keV/keV
10^14
10^13
10^12
10^11
10^10
10^9
10^8
0
10
20
30
40
50
60
hν, keV

Figure 17

MICRODENSITOMER SCANS OF TIME DELAY SERIES

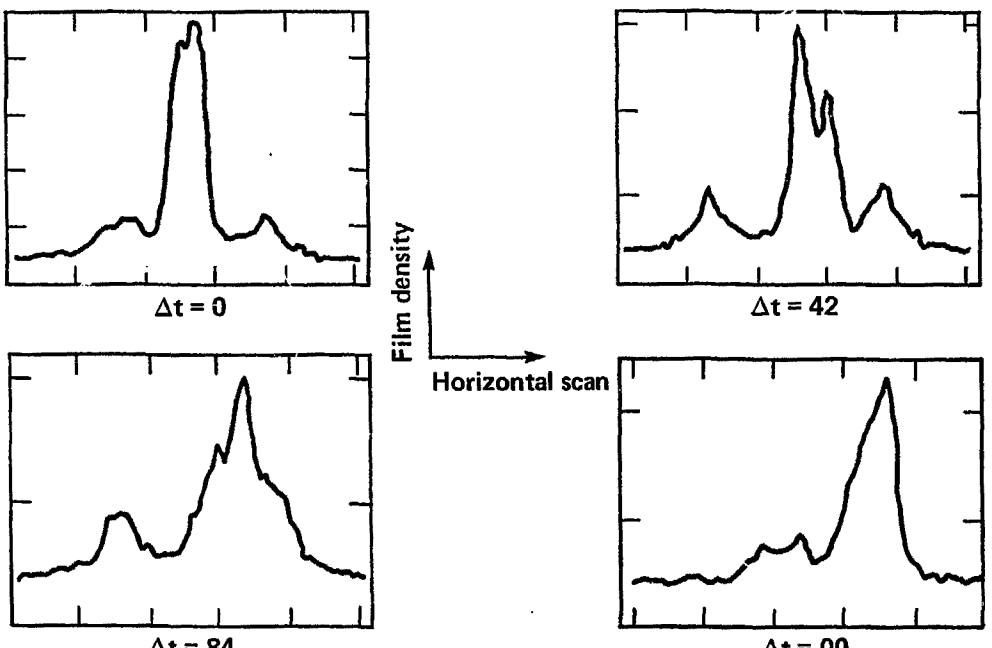

Figure 18

MOTION OF STAGNATION REGION PROVIDES MEASUREMENT OF AVERAGE IMPLOSION VELOCITY

Δt = Beam delay in psec

Δx = Displaeement of stagnation region from center of sphere

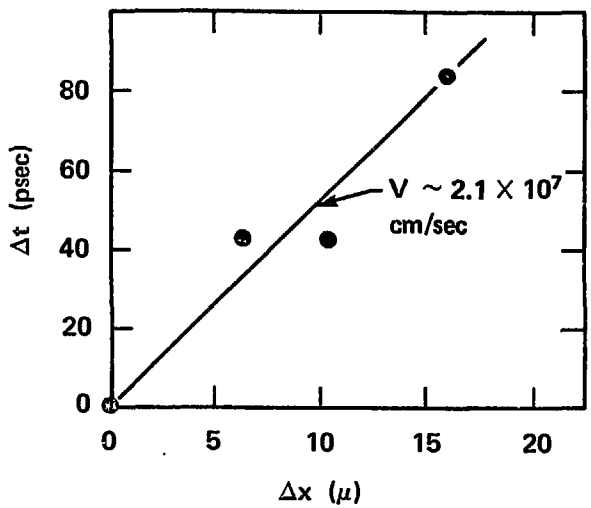

Figure 19

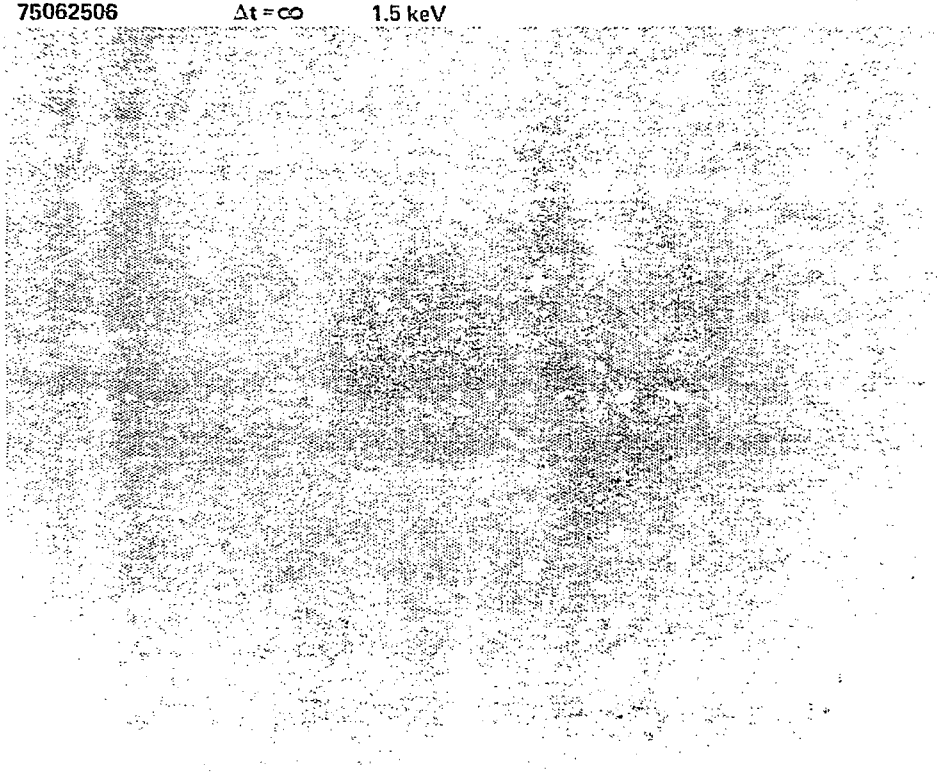

Figure 20

THE SCATTERED LIGHT ANGULAR DISTRIBUTION SHOWS POLARIZATION DEPENDENCE

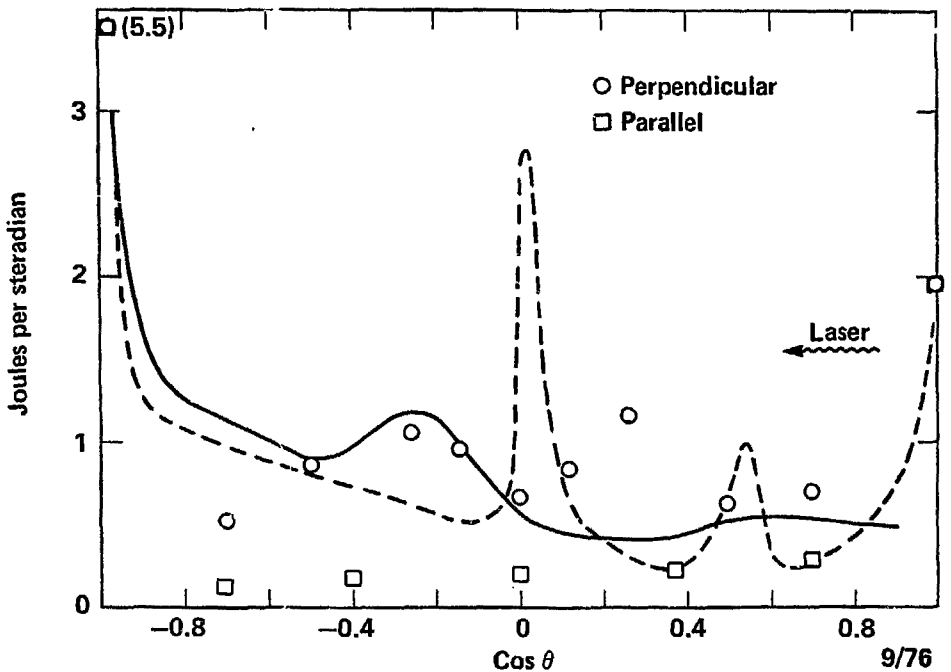

Figure 21

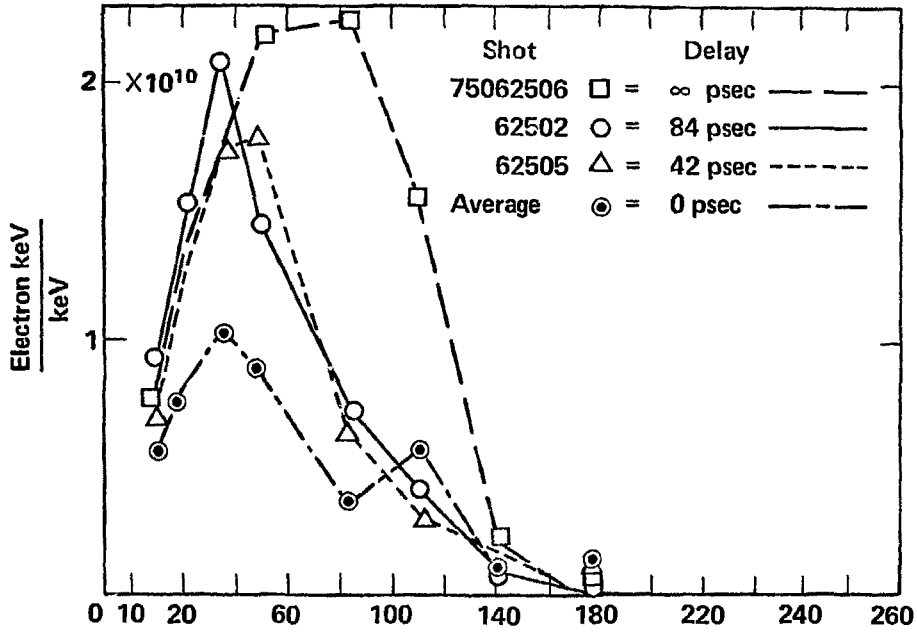
Shot
Delay
75062506 □ = ∞ psec
62502 ○ = 84 psec
62505 △ = 42 psec
Average ◉ = 0 psec
X10¹⁰
Electron keV / keV
2
1
0 10 20 60 100 140 180 220 240 260

Figure 22

VARIATION OF DT FILL AFFECTS THE COMPRESSION EFFICIENCY IN EXPLODING PUSHER EXPERIMENTS

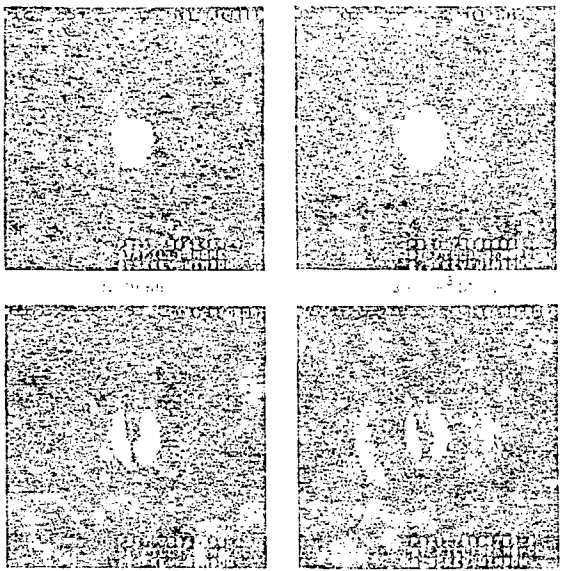

FIGURE 25

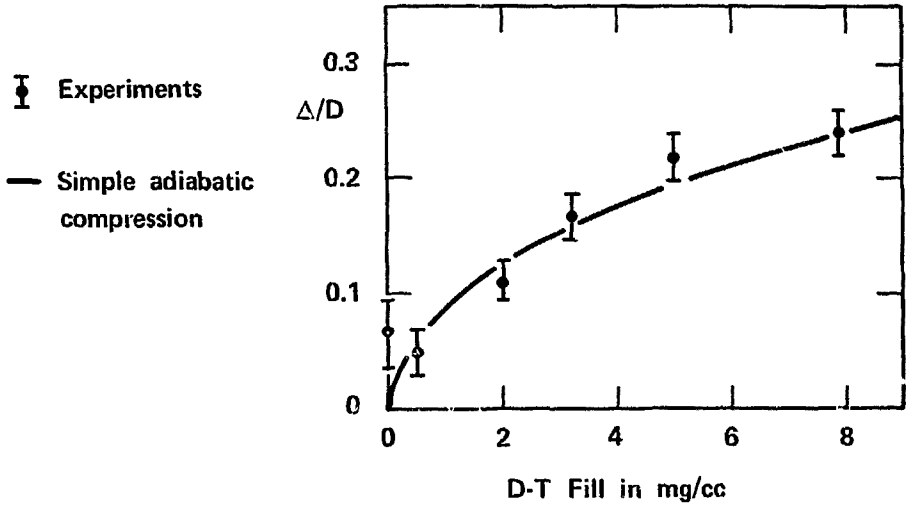
Experiments
Simple adiabatic compression
0.3
Δ/D
0.2
0.1
0
0
2
4
6
8
D-T Fill in mg/cc

Figure 24

At low pressure
N ~ fill

At high pressure
N ~ (fill)$^{-2}$

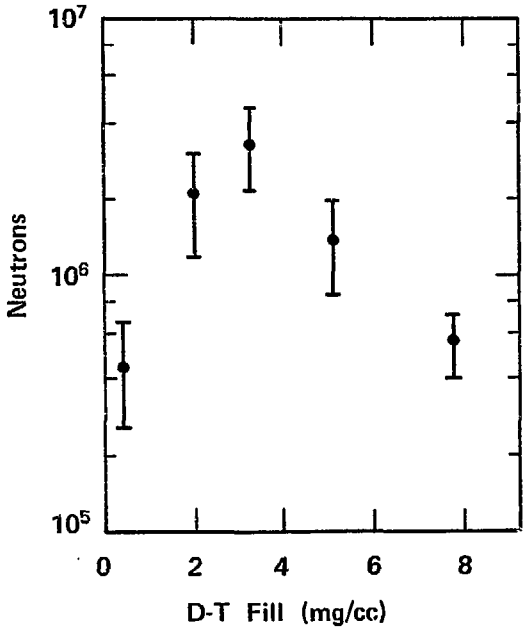

Figure 25

THE IMPLOSION SYMMETRY IS DEPENDENT ON INCIDENT LASER INTENSITY (W/cm^2)

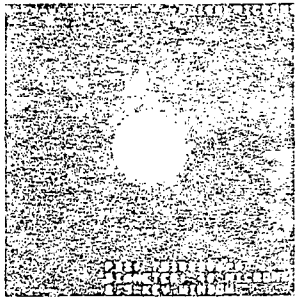

40-μm ball, 3.8 · 10^{15} W/cm^2

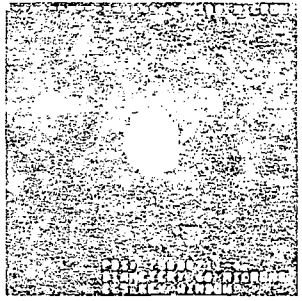

60-μm ball, 1.5 10^{16} W/cm^2

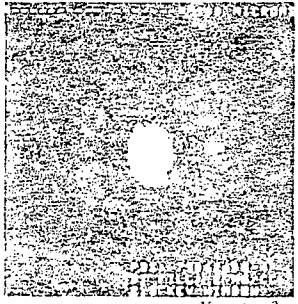

80-μm ball, 7.8 · 10^{14} W/cm^2

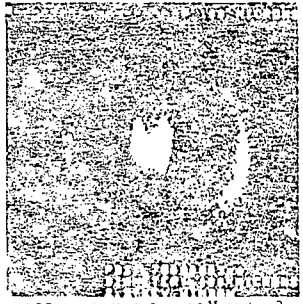

100-μm ball, 3.8 · 10^{15} W/cm^2

9-76

Figure 26

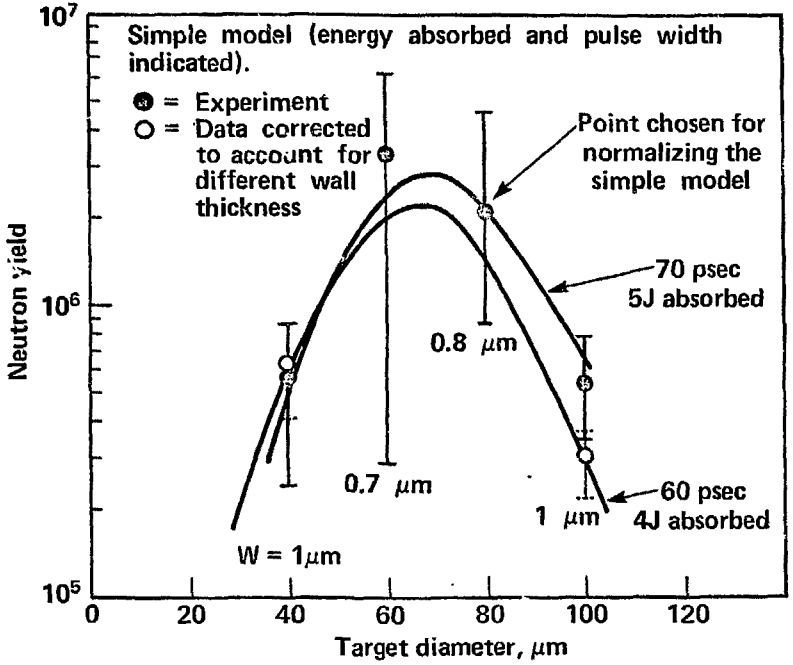

9/76

Figure 27

ABSORPTION OF INCIDENT 1.06 μ LASER LIGHT AVERAGES TO ~27% FOR EXPLODING PUSHER TARGETS

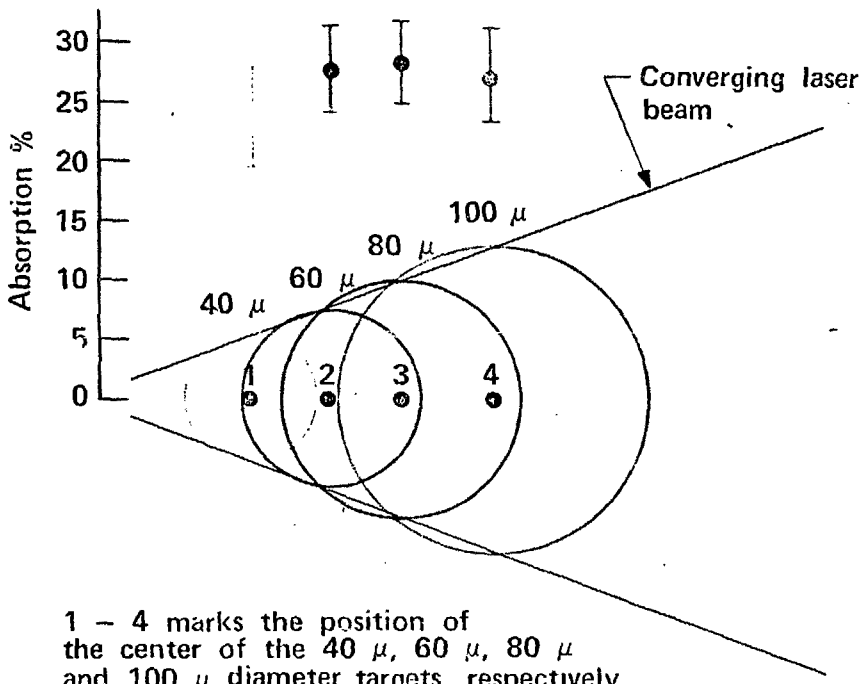

1 – 4 marks the position of the center of the 40 μ, 60 μ, 80 μ and 100 μ diameter targets, respectively

Figure 28

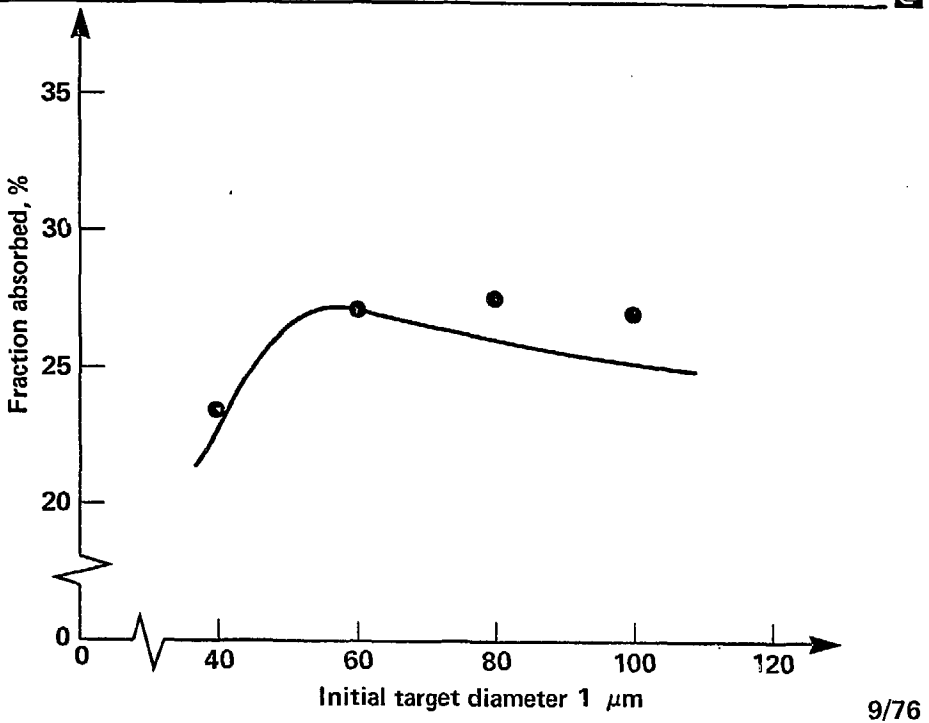
35
30
25
20
0
Fraction absorbed, %
0
40
60
80
100
120
Initial target diameter 1 μm
9/76

Figure 29

Figure 30

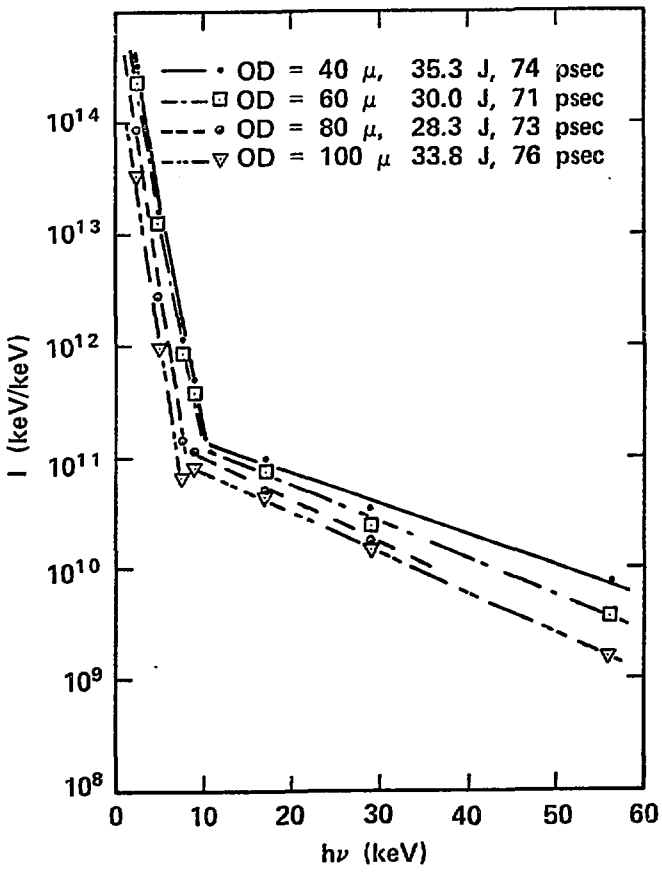
OD = 40 μ, 35.3 J, 74 psec
OD = 60 μ 30.0 J, 71 psec
OD = 80 μ, 28.3 J, 73 psec
OD = 100 μ 33.8 J, 76 psec
I (keV/keV)
10^14
10^13
10^12
10^11
10^10
10^9
10^8
0
10
20
30
40
50
60
hν (keV)

PROOF OF THERMONUCLEAR REACTION

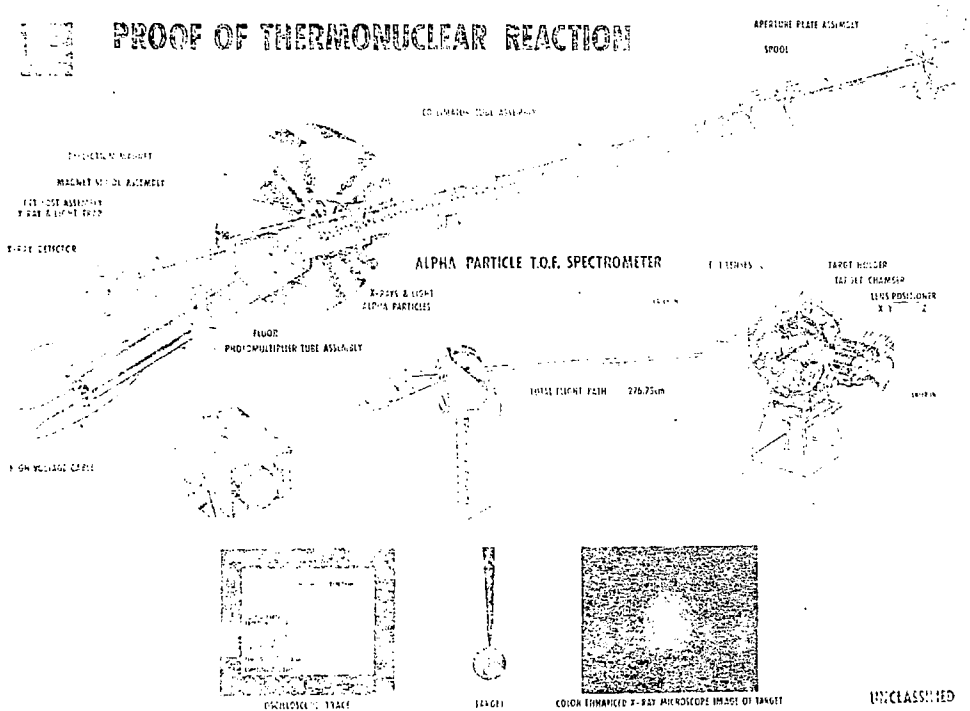

UNCLASSIFIED

Figure 31

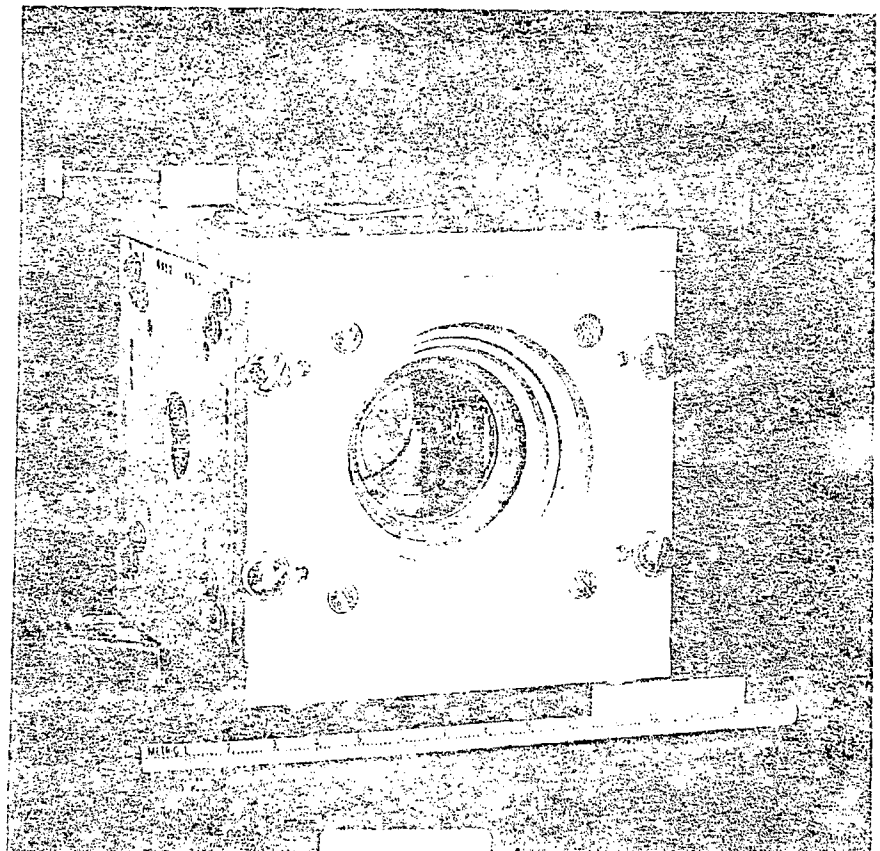

FIGURE 32

CONSTRUCTION OF THE BOX CALORIMETER

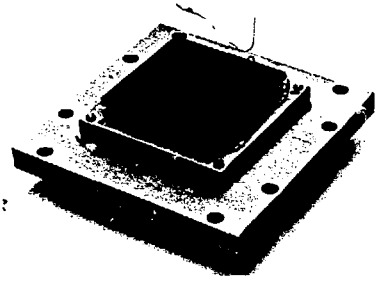

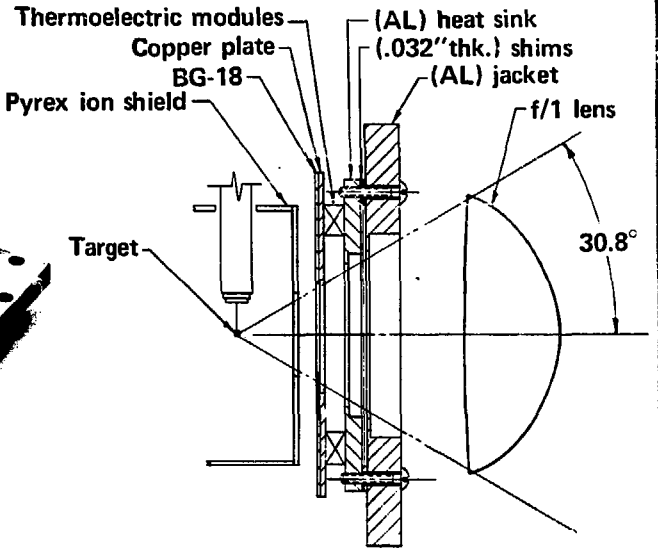

FIGURE 33